

Development of a Hybrid Electric Traction Platform for Agricultural Machinery

by

Abass Afolabi Yahaya



Submitted to the Department of Electrical Engineering, Electronics,
Computers and Systems
in partial fulfillment of the requirements for the degree of
Erasmus Mundus Master Course in Sustainable Transportation and
Electrical Power Systems

at the

UNIVERSIDAD DE OVIEDO

September 2018

© Universidad de Oviedo 2018. All rights reserved.

Author

Certified by

Pablo García Fernández
Associate Professor
Thesis Supervisor

Development of a Hybrid Electric Traction Platform for Agricultural Machinery

by

Abass Afolabi Yahaya

Submitted to the Department of Electrical Engineering, Electronics, Computers and
Systems

on September 01, 2018, in partial fulfillment of the
requirements for the degree of

Erasmus Mundus Master Course in Sustainable Transportation and Electrical
Power Systems

Abstract

Electricity is the new fuel and the preferred form of energy for the future. Electricity has revolutionized, not just domestic energy consumption, but also in transportation energy usage. Fossil fuels are non-sustainable and causes global warming, hence, hybrid electric and fully-electric vehicular means of transportation will replace the conventional fossil-fueled types. In this thesis, a series hybrid electric vehicle platform is designed and developed for usage in autonomous agricultural machine applications. Energy Management System scheme is designed to apportion primary energy usage between electrical and mechanical works, and the integration and control of battery energy storage system is also implemented. The control systems of the electric motors running the wheels are designed and integrated with an auto-path trajectory tracking scheme for autonomous operation mode. A series of simulations have been carried out to test effectiveness of the implemented algorithms. Practical hardware laboratory build-up of the proposed platform topology has been implemented from the scratch.

Thesis Supervisor: Pablo García Fernández

Title: Associate Professor

Acknowledgments

My greatest admiration goes to the European Union for creating the Erasmus Mundus Scholarship platform and to administer the European academic exposure and opportunity to humanity. It is also with delight that I appreciate the coordinating universities of my program, Erasmus Mundus Master Course in Sustainable Transportation and Electric Power Systems (EMMC-STEPS), for providing me with indelible academic sojourns and cultural demeanour of several countries; University of Oviedo in Spain, University of Nottingham in United Kingdom, and Polytechnic Institute of Coimbra in Portugal. I will also like to appreciate SVMAC Engineering Systems and Vehicles (SVMAC Ingeniería Sistemas y Vehículos) for sponsoring this project.

I candidly appreciate the efforts and erudition of my thesis adviser, Prof. Pablo García Fernández, for his untiring services in pointing me in the right academic directions and his lavish expenditure of time in delineating electrical principles to me. I also acknowledge his recognition of my efforts, and ability to work independently and as a group member and his selflessness in discussing my academic future with me. I will also like to thank other Professors in the Program, especially Professor Jorge Garcia for giving me permissions to audit some of his classes. It is morally compulsory for me to heartily thank the amiable EMMC-STEPS Administrative Organization Officer, Susana Menéndez Bustillo, for the speed, efficiency and happiness she expends in solving students' issues. Susana is first-class.

Furthermore, I will to acknowledge my family for their emotional support and encouragement however far or continent-away that they may be. I cannot but appreciate the support I received from my senior colleagues during my laboratory implementation; Andres, Sarah, Angel, Geber, and Carlos. All were wonderful in handing down there former experience with some equipment and procedures. I will also like give regards to my classmates, EMMC-STEPS 2016-18 Set, for all the fun, differences, cultures and camaraderie that we shared.

Contents

1	Thesis Introduction	15
1.1	Introduction	15
1.2	Objectives	16
1.3	Thesis Structure	17
2	Literature Review	21
2.1	EV and HEV Architectures	21
2.2	The Choice of PMSM for Electric Vehicles: Trends and Challenges . .	24
2.3	Structures of PMSMs	27
3	Hybrid Platform Design	31
3.1	Introduction	31
3.2	Proposed Multi-Machine HEV Topology	31
3.2.1	System Design	34
3.3	Energy Management System	38
3.4	Battery Charge Controller	39
3.4.1	Operation of Bidirectional DC-DC Boost Converter	40
3.4.2	Average Model of Bidirectional DC-DC Boost Converter . . .	42
3.4.3	Battery Current Controller Design	45
3.5	Energy Management Simulations	46
3.6	Conclusion	52
4	Differential Drive Vehicle Analysis and Trajectory Control	53

4.1	Introduction	53
4.2	Differential Drive Kinematics	53
4.3	Vehicle Dynamics	55
4.4	Trajectory Tracking Controller Design	58
4.5	PMSM Dynamic Modeling and Control	60
4.5.1	Current Controller Design	62
4.5.2	Speed Controller Design	63
4.6	Path Tracking Simulation Results	64
4.7	Conclusion	72
5	Experimental Set-Up	77
5.1	Platform Assembly	77
5.2	Experimental Results	81
6	Conclusions and Future Works	83
6.1	Conclusions	83
6.2	Future Works	84
A	Tables	87
B	Figures	89

List of Figures

2-1	Series HEV topology	22
2-2	Parallel HEV topology	22
2-3	Topology of ISG based HEV	23
2-4	Topology of split-type in-wheel drive	23
2-5	B-H characteristics of Permanent Magnets	24
2-6	Comparison of permanent magnets	25
2-7	Evaluations of the suitability of electric motor types for HEV	26
2-8	Energy loss over New European Driving Cycle	26
2-9	Different types of Permanent Magnet Rotor Designs	28
2-10	Common PMSM configurations	29
2-11	D-Q axis depiction of common PMSMs	29
2-12	Ratio of reluctance and magnetic torques in PMSMs	30
3-1	Proposed topology of series HEV	32
3-2	Mechanical hydraulic scheme	35
3-3	Forces required for vehicle motion	36
3-4	Velocity profile of the vehicle at different landscapes	37
3-5	The state of charge of battery as it discharges into PMSM	38
3-6	Energy Management Scheme for the HEV	39
3-7	Bidirectional boost converter topology	40
3-8	Working of bidirectional boost converter in boost mode	41
3-9	Working of bidirectional boost converter in buck mode	42
3-10	Operating cycle of average model of bidirectional boost converter	43

3-11	Average model of bidirectional boost converter	44
3-12	Battery current control loop scheme	46
3-13	Power Ratings of primary equipment	47
3-14	Generator power limits and, Generator and Battery power at no motor load	47
3-15	Generator power limits and power output with motor-power demand	48
3-16	Generator and battery power meeting motor-power demand	48
3-17	DC-Link voltage response during motor-power demand	49
3-18	Currents at dc-link node during motor-power demand	50
3-19	Generator currents at generator terminal	50
3-20	Battery power output and reference	51
3-21	Battery Current output and reference at battery terminal	51
3-22	Duty cycle of battery and generator converters	52
4-1	Vehicle kinematics parameters with ICC	54
4-2	Vehicle front-side and global coordinates parameters	55
4-3	Parameters for wheel and motor dynamics in a dual-motor driven vehicle	56
4-4	Trajectory tracking with destination waypoint	58
4-5	Trajectory tracking scheme and procedure	60
4-6	Basic vector control scheme of the PMSM	61
4-7	PMSM synchronous reference frame model with coupling	62
4-8	Current controller design with feedforward term for decoupling	63
4-9	Speed controller design with additional feedforward terms	64
4-10	Vehicle motion in Case I algorithm	65
4-11	Angular difference in motion of Case I algorithm	65
4-12	Vehicle motion in Case II algorithm	66
4-13	Angular difference in motion of Case II algorithm	67
4-14	Error inputs into trajectory tracking controllers	67
4-15	Linear and angular velocities of vehicle	68
4-16	Linear and angular acceleration of vehicle	68

4-17	Linear and angular jerk of vehicle	69
4-18	Speed of PMSM motors of vehicle	69
4-19	Vehicle position in global coordinates with next-point commands	70
4-20	Torque of right and left electric motors of vehicle	70
4-21	Current of left motor of vehicle	70
4-22	Current of right motor of vehicle	71
4-23	Voltage of left motor of vehicle	71
4-24	Voltage of right motor of vehicle	71
4-25	Vehicle motion in case of real farmland trajectory	74
4-26	Angular difference in case of real farmland trajectory	74
4-27	Speed of PMSM motors of vehicle in case of real farmland trajectory	75
5-1	Entire platform with all accessories	79
5-2	Engine, generator and motor bench	79
5-3	DC/AC inverter, master controller and remote controller bench	80
5-4	DC/DC converter and battery bench	80
5-5	Commercial electric drive for prime mover	81
5-6	Experimental results	82
B-1	Internal features of SKAI2 LV A2 MM10-L MOSFET inverter	89
B-2	Package outlook of SKAI2 LV A2 MM10-L MOSFET inverter	90
B-3	Dual three-phase MOSFET inverter as connection point for the PMSMs	90
B-4	ACM BRL110-3D 6 Poles Permanent Magnent Synchronous Electric Motor	91
B-5	Sincro FB 4-48/150 Brushless Synchronous Generator with DC output	91

List of Tables

2.1	Comparison of PMSM, IM and SRM for EV/HEV Purposes	27
A.1	Bi-directional DC/DC Converter Parameters	87
A.2	Permanent Magnet Synchronous Motor Data	87
A.3	Vehicle and Dynamics Data Used in Simulation	88
A.4	Controller Design Parameters	88

Chapter 1

Thesis Introduction

1.1 Introduction

It is expected that human energy needs will keep growing in decades to come, hence, it is appropriate that energy is used in most efficient way without hazardous consequences. Literature has it that fossil fuel, a common primary source of energy, is without doubt unsustainable and limited in availability. Furthermore, it is associated with global warming, greenhouse gases emission, rise in ocean levels, melting of glaciers, and depletion of ozone layer among other hazardous effect; Holocene Temperature Variation Graph, Global Land-Ocean Temperature Index, Keeling Curve [1, 2]. Several investigations and research through time has tenable facts and proofs to the claim. However, the world dependence on petroleum product is still immense, although trying to reduce this dependency, coal still produces 28%, oil 33% and natural gas 24% of world energy source [3].

Of the total world energy produced, it is known that about 25% of the usage goes into the transportation sector; the USA uses 29% and Europe uses 33% of total energy in transportation [3, 4, 5]. And of these, more than 90% is provided by petroleum products in all cases [3, 4, 5]. With the efficiency of internal combustion engines as low as below 40%, it is imperative that alternatives be sought and developed. This, with earlier mentioned derogatory factors associated with fossil fuels, have given incentives into researches for alternatives such as hybrid electric vehicle and full electric

vehicles. Presently, electricity usage in transportation is about 5% mostly from train transportation [3, 4].

Several efforts are ongoing in increasing the share of electric mobility for road transportation and in agricultural works. In agriculture, electric vehicle will increase farmers efficiency and productivity as several projects are on going for unmanned agri-bots and autonomous agricultural vehicles. This will ease meeting of new pollution laws and carbon emission limits. This thesis focuses on the design of a series hybrid electric platform for use in an agricultural environment which will work at a capacity of 18kW distributed between mechanical works and 48V dc-link inverter function. The mechanical work, in full capacity, can demand 15kW while the electrical demand is limited by the 7.2kW rating of the generator. However, the complementary demand profile of the mechanical and electrical works in this application coupled with proper energy management system design and integration of batteries sized 2.13kWh makes the system a reality. In other words, when cutting thick grasses there is no need for high motor acceleration and vice versa.

1.2 Objectives

The main theme of this thesis is to contribute to the expanding vastness of electric vehicle applications into the agricultural endeavour. This will be done in this thesis by proposing to design a hybrid electric vehicle platform for agricultural applications. More so, the design of trajectory path tracking is simplified, and the thesis puts together several electrical engineering technologies for the purpose. The platform is designed for autonomous and remote-controlled operations and has geolocation and planning abilities. This is inline with enabling Industry 4.0 standards in agricultural practices. Therefore, the objectives set-forth for the proposed studies in this thesis are listed below:

- **Hybrid Platform Design:** The design of the hybrid platform entails the choice of series hybrid electric vehicle and the particular component design. The function of each component of the design is detailed and the mode of in-

teraction between them. The platform will be designed for autonomous and remote-controlled operations and the particular chosen mode will be implemented. More so, how all the components will be physically interconnected.

- **Design of Control System:** Several layers and levels of control details are proposed and designed. An Energy Management System scheme is proposed which further entails the design of control systems for DC/DC and DC/AC converters. The control and speed control loop for each electric motor will be designed and integrated with the control design of autonomous path trajectory tracking using proportional-derivative controllers, which is also being proposed. The system will be tested via Matlab/Simulink simulation environment.
- **Experimental Implementation of Hybrid Platform:** The proposed hybrid platform will be hardware-implemented in laboratory environment putting together all available components; internal combustion engine, electric power generator, DC/AC and DC/DC converters, Permanent magnet synchronous motors and battery energy storage systems. The control systems will be implemented and tested on the hardware equipment. The performance of the system will be validated.

1.3 Thesis Structure

In order to aptly report on the success attained in achieving the objectives laid out in section 1.2, this thesis report has been divided into several chapters and sections. The chapters are listed below with summaries of their contents.

- **Chapter 1: Introduction.** This chapter introduces into the thesis by providing the motivations behind the thesis proposal. It also details the objectives to be attained in the thesis and gives an overview of each chapter of this report.
- **Chapter 2: Literature Review.** This gives account of past literature on the applications and current issues about machinery used in this work. it provides review of the several topologies of hybrid electric and full electric vehicles

available. Chapter 2 also details the popularity and suitability of several candidate electric motors in electric vehicle applications, the controversies behind the popular choice of permanent magnet synchronous machines (PMSM) due to the cost of Neodymium magnets, and the drive for alternatives. The structure of the PMSM is reviewed and the proposed dual-motor series hybrid electric vehicle platform is introduced.

- **Chapter 3: Energy Management System.** This chapter concentrates on the development of an Energy Management System for distribution of power flow from the internal combustion engine to mechanical pump, electric generator, electric motors and the battery. It also details the control of the battery power flow via a bidirectional dc-dc boost converter in the boost mode and the buck mode. The principles of the average model of this converter is detailed and used in simulation. The dc-link voltage control via the dc-dc converter adjacent to the generator is also explored. Simulation results detailing performance of the algorithm is presented.
- **Chapter 4: Differential Drive Vehicle Analysis and Trajectory Control.** This chapter takes on the motion features of the vehicle. It details the vehicles differential drive kinematics translating the wheel speeds into the vehicle body linear and rotational speeds and vice versa. The chapter also contains the dynamic analysis of the electric motors with the wheels, and integrates it with the dynamic motion analysis of the vehicle as an entity. The torque equation required by each electric motor is obtained and employed in designing the motor speed control. The trajectory tracking controller is also designed in this chapter. Several simulation results are presented.
- **Chapter 5: Experimental Implementation.** This gives details of the experimental implementation of the hybrid electric vehicle in a laboratory environment. The details of the hardware equipment used in the set-up are given and experimental results are presented and explained.

- **Chapter 6: Conclusions and Future Works.** The concluding chapter gives final remarks about the thesis in the conclusion section and gives details of possible future paths into expanding and improving the proposed schemes.

Chapter 2

Literature Review

2.1 EV and HEV Architectures

Electric and hybrid electric vehicles have received so much political, and academic attention in recent years leading to the apparent huge research funding in this direction. The most common HEVs and EVs utilize the centralized power layout or single machine system in which a single mechanical shaft supplies the entire motive power of the vehicle [6]. EV are usually series in nature while HEV are more flexible with several topology options; series, parallel, series-parallel and complex hybrid. EVs usually contain a single energy source such as Battery EV (BEV) and fuel cell EV (FCEV), while hybrids contain more than one energy source with which internal combustion engine is a common source. Series and Parallel HEV topologies are given in Figures 2-1 and 2-2.

A successful boost to the family of hybrid electric vehicle is the integrated starter-generator (ISG) system in which an electric machine is mounted on the crank between the ICE and the clutch-gear box assembly [7]. The ISG aids the vehicle in fuel economy and reduced emissions has it start-up the ICE, supports motors during intermittent driving cycles and enables regenerative braking [6, 7]. The topology of ISG based HEV is given in Figure 2-3

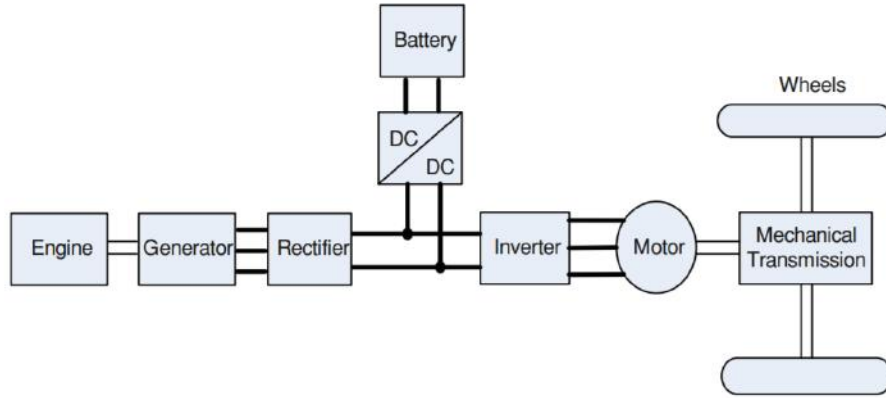


Figure 2-1: Series HEV topology [8]

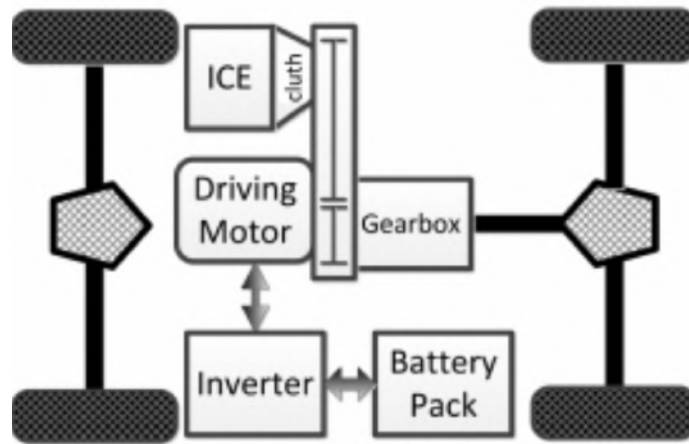


Figure 2-2: Parallel HEV topology [6]

Literature also has other advanced topologies of electric vehicles using multiple machines as the vehicle motive power. Also several hybrid energy storage systems have been proposed for electric vehicles [9]. Topologies such as wheel drive system, two-machine system for HEV, multi-motor drive systems and compound-structure integrated machines system have been proposed [6]. Dual-motor HEV do have higher efficiency and higher electric drive ability making them more powerful but usually at the cost of complexity in control and design. The wheel drive system mounts the electric motor inside the wheel of the vehicle, thereby, having the advantages of compactness, lighter weight by precluding the clutch, gearbox and transmission. The motors can drive the wheel directly or indirectly which will require two or four electric

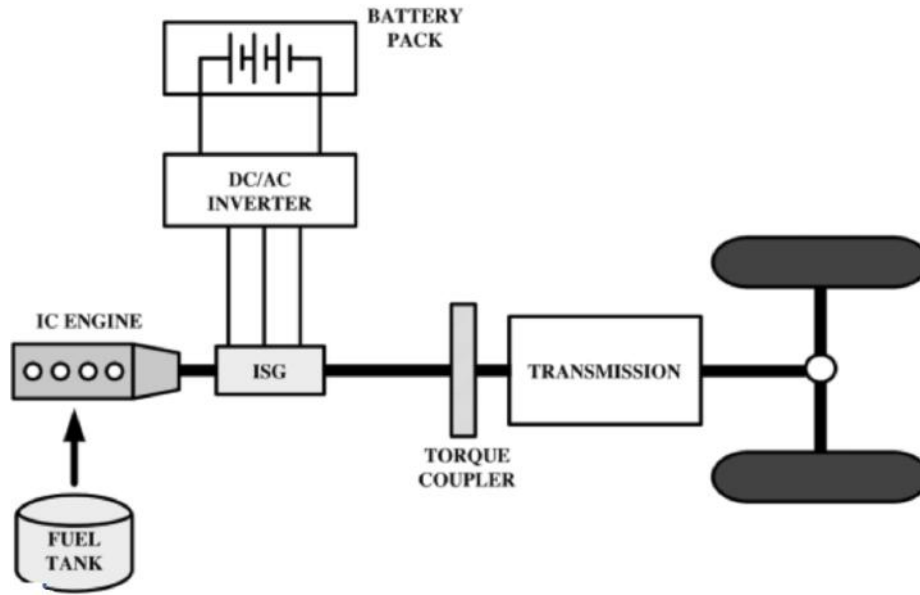


Figure 2-3: Topology of ISG based HEV [7]

motors to implement. A complex type of the direct in-wheel drive is the split-type in which the vehicle can be driven by two types of motive power but via different connections and wheels. Figure 2-4 shows a split type in-wheel direct drive electric vehicle.

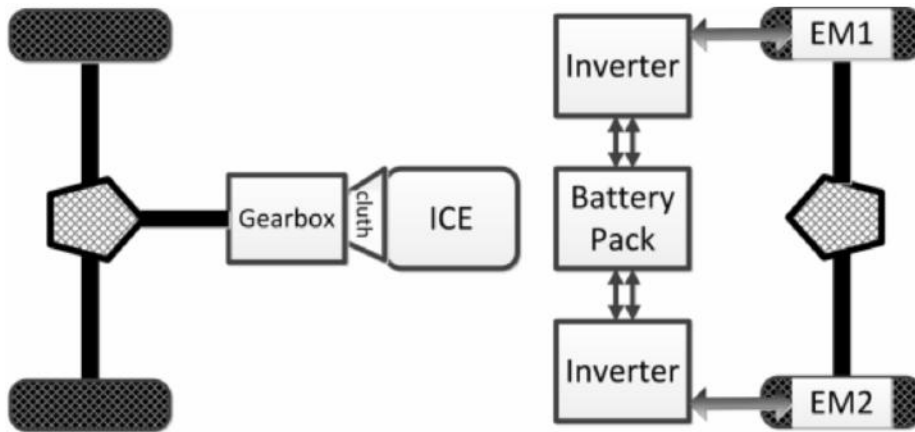


Figure 2-4: Topology of split-type in-wheel drive [6]

It is chosen that the preferred design topology for this thesis work is on the series HEV basis. But the wheels on the vehicle will be driven by individual electric motors, as-in a dual-machine system, and will be indirectly driven via reduction gears. The

power ports for the motors will be via an ICE-generator connection and battery set.

2.2 The Choice of PMSM for Electric Vehicles: Trends and Challenges

The most common permanent magnets used in electric motors are Ferrites or Ceramic, Alnico and rare-earth magnets, and the strongest are the rare-earth magnets; Samarium-Cobalt (SmCo) and Neodymium-Iron-Boron (NdFeB). Although Alnico and Ferrites can maintain their magnetism at higher temperature, NdFeB magnets have been the most widely used due to superior residual flux density and coercivity as depicted in Figure 2-5. The high energy product, i.e BH_{max} , means higher power density, higher flux density per weight, lower inertia, higher dynamic response, no rotor copper loss, and higher efficiency for the PMSMs. On the otherhand, NdFeB have demerits such as high cost, low operating temperature and can corrode easily. Figure 2-6 uses bar graphs to compare the strengths and weaknesses of each permanent magnet type.

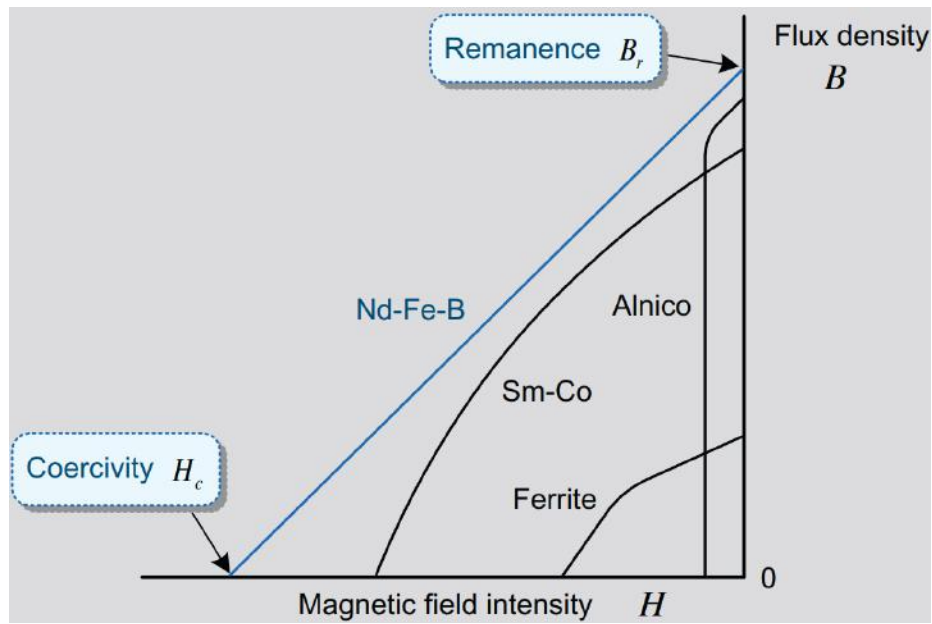


Figure 2-5: B-H characteristics of Permanent Magnets [10]

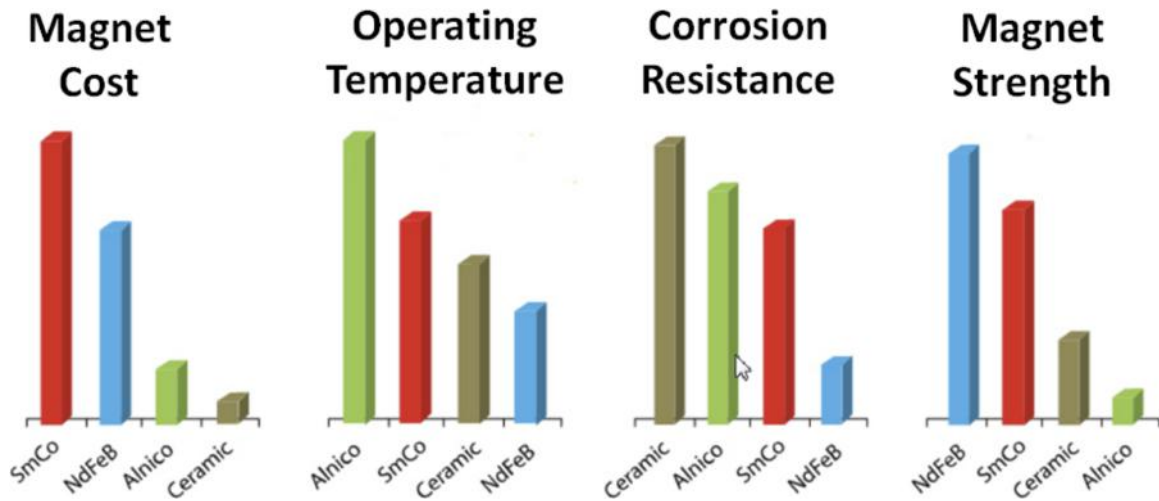


Figure 2-6: Comparison of permanent magnets [11]

Studies have been made to select the most generally suitable electric motor types while other studies focused on best geometry of PMSMs for optimal performance in electric vehicles (EV) and hybrid electric vehicles (HEV)[12, 13, 14, 15]. Zeraoulia *et al* ranks DC, induction motors (IM), PMSM, and switched reluctance motor (SRM) based on affordability, efficiency, flux-weakening capability and reliability to provide required traction for parallel HEV, and their convictions are captured in Figure 2-7 where higher digits means merits. However, majority of new researches in literature favours the superiority of PMSMs as most suitable for EVs and HEVs regardless of the cost while some maintain that selections are requirement-based. Table 2.1 details the merits and demerits of these motors [14]. Furthermore, in Figure 2-8 the temperature loss of IM, surface-mounted and internal PMSMs were measured based on New European Driving Cycle requirements, while Table 2.1 shows the comparison between the different types of PMSMs for EV/HEV usage.

However, the future of PMSMs and machines used in EV/HEV is not entirely for rare-earth magnets as there are intense research for alternative high performance motors. These alternatives involve harvesting and recycling of e-waste permanent magnets, developments of motors with low or zero amount of permanent magnets, and some focus on using ferrites [16, 17, 18, 19]. The European Union sponsored ARMEVA (Advanced Reluctance Motors for Electric Vehicle Applications) program

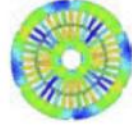
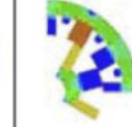
<i>Propulsion Systems</i>				
<i>Characteristics</i>	DC	IM	PM	SRM
<i>Power Density</i>	2.5	3.5	5	3.5
<i>Efficiency</i>	2.5	3.5	5	3.5
<i>Controllability</i>	5	5	4	3
<i>Reliability</i>	3	5	4	5
<i>Technological maturity</i>	5	5	4	4
<i>Cost</i>	4	5	3	4
Σ Total	 22	 27	 25	 23

Figure 2-7: Evaluations of the suitability of electric motor types for HEV [12]

focuses on development of high performance SRM to stop dependence on China-controlled rare-earth market [20].

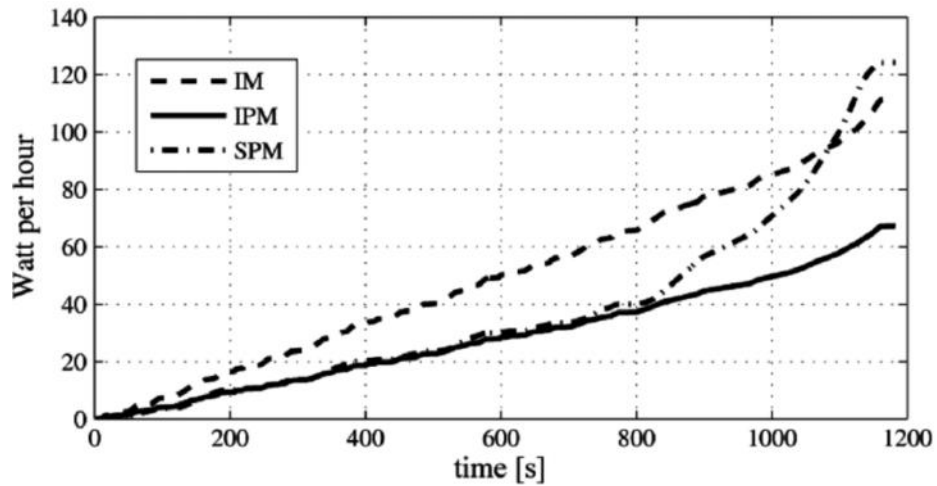


Figure 2-8: Energy loss over New European Driving Cycle [13]

Table 2.1: Comparison of PMSM, IM and SRM for EV/HEV Purposes

PMSM	Induction Motor	SRM
Advantages		
<ul style="list-style-type: none"> • Wide torque speed range • High power density • High torque density 	<ul style="list-style-type: none"> • No magnets • Robust 	<ul style="list-style-type: none"> • No magnets • Most Robust • Fault tolerant
Disadvantages		
<ul style="list-style-type: none"> • High cost • Rare-earth availability 	<ul style="list-style-type: none"> • High heat loss 	<ul style="list-style-type: none"> • Low pf • Acoustic noise • High torque ripples

2.3 Structures of PMSMs

In general, synchronous motors require separate excitation for stator (armature) and rotor (field winding) which differs markedly from the popular induction motor which is singly excited via its stator. The division of synchronous motors that employ permanent magnets on or inside their rotors are called permanent magnet synchronous motors (PMSM) which are classified based on arrangement of the rotor magnets; Surface-mounted PMSM, Surface-inset PMSM, interior PMSM, V-shaped internal PMSM, and Radial-internal PMSM [21]. The rotor structures of these PMSMs are shown in Figure 2-9. To show the effect of rotor structures on performance of PMSM, Dimitar et al [22] and Gaurang et al [23] have used metrics such as profiles of air-gap flux, generated torque, cogging torque, ripple and average torque, back-EMF and its THD of similarly rated differently configured PMSMs as a means of performance comparison. Surface-mounted PMSM have highest operating flux density, but also highest flux leakage which contributes to their more trapezoidal flux profile than others, better back-emf and less cogging torque. The interior PMSM has good performance for a wide speed range but utilization of core and magnet materials is poor, while the

radial-internal PMSM has the worst performance.

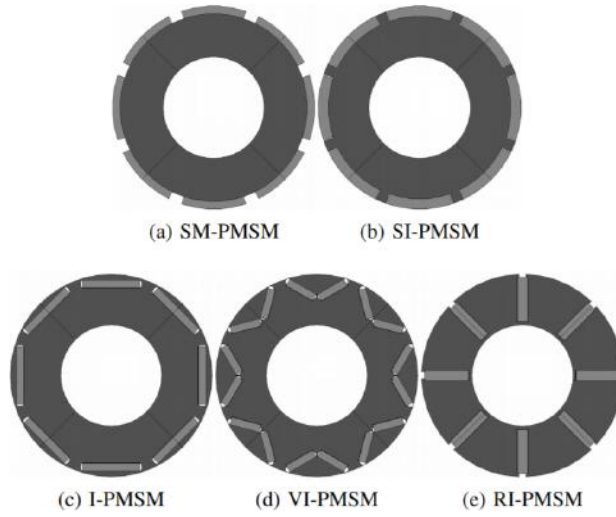


Figure 2-9: Different types of Permanent Magnet Rotor Designs [21]

PMSM can also be categorized based on flux direction which are mainly axial-flux, radial-flux, axial/radial-flux PMSMs [10],[24]. The most common is the radial-flux type where the rotor rotates inside the stator, while in axial-flux types the rotor rotates outside the stator as shown in Figure 2-10. However, literature has it that axial-flux machines have higher torque density than radial-flux types, while torque density of the axial/radial-flux types depends on specific built configurations [24]. Compound-structure PMSM (CS-PMSM) which integrates two PMSMs have been proposed. CS-PMSM are formed from the three basic PMSMs, hence it has six possible configurations with each having two independent mechanical output shafts originating from its dual rotor and a stator machine [24].

Furthermore, magnet arrangement affects the dynamics of PMSMs as it affects the d-q axis components of stator inductance which is vital in electromagnetic analysis, and the depiction of some common PMSMs via d-q axis are given in (2.1). Magnetic saliency exist if the d-q axis components of inductance are not the same. It is important to note that the permeability of rare earth magnets being equivalent to that of air gives more credence to arrangements of magnets as core in PMSM analyses via rotating reference frame. For example, these saliency affects the torque generated by

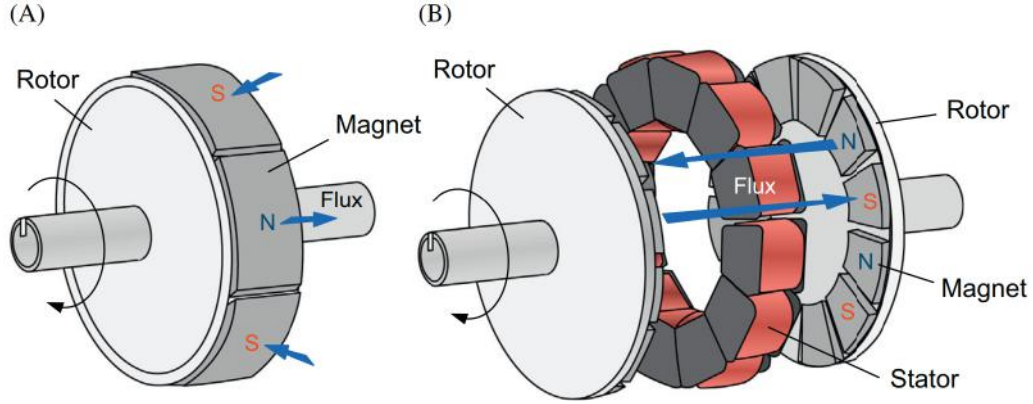


Figure 2-10: Common PMSM configurations (A) Radial-flux PMSM and (B) Axial-flux PMSM [10]

PMSMs which is either based on magnetism of the permanent magnets, reluctance due to saliency of rotor shape or both. The expression for this torque is given in (2.1) where the first term is magnetic and the second term is the reluctance part [21]. Figure 2-12 depicts a comparison among brushless motors as regards the proportion of total torque gained due to reluctance and magnetism.

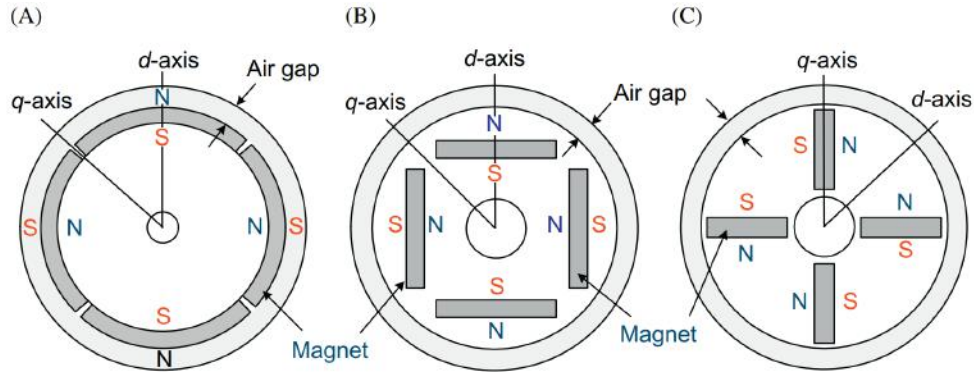


Figure 2-11: D-Q axis depiction of common PMSMs (A) SM-PMSM, (B) IPMSM, and (C) RI-PMSM [10]

$$T = \frac{3}{2}P * i_q * [\psi_{pm} + (L_d - L_q) * i_d] \quad (2.1)$$

where T is the torque generated by motor, P is the number of poles, i_d and i_q are the direct and quadrature components of the stator currents, ψ_{pm} is the permanent magnet flux, and L_d and L_q are the direct and quadrature components of motor

inductances.

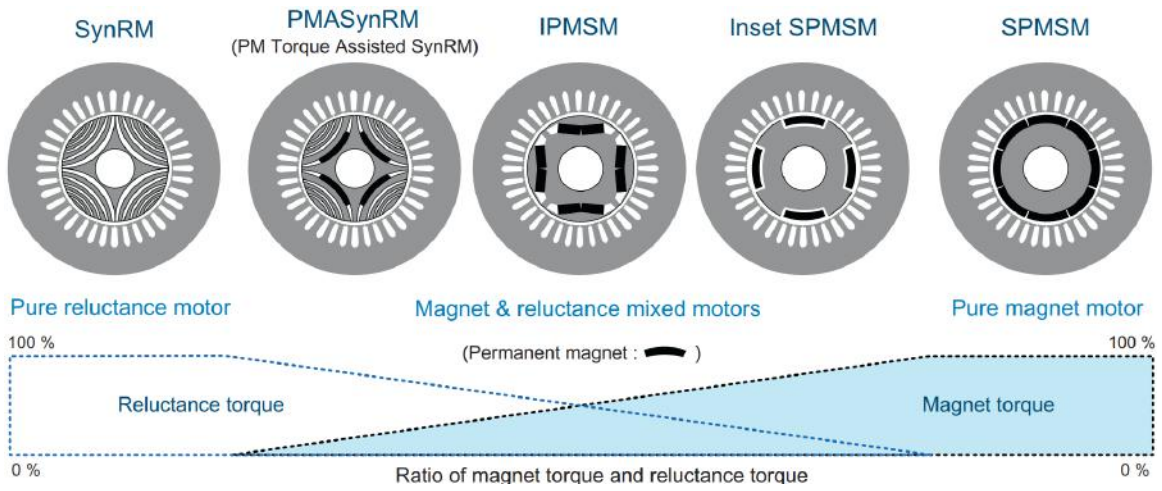


Figure 2-12: Ratio of reluctance and magnetic torques in PMSMs [10]

Chapter 3

Hybrid Platform Design

3.1 Introduction

This chapter gives description of the proposed series HEV topology, explanation of the proposed power flow, and power management for the entire vehicle system. It details how the internal combustion engine which is the primary energy source will apportion its available energy and the priority list for the components. Furthermore, details of how the battery source interacts with the entire system, its discharging and charging via dc-dc boost converter, and usage of the average model and control are exploited.

3.2 Proposed Multi-Machine HEV Topology

The proposed scheme is a dual-motor driven series HEV with several components interacting via lines of communication, control and power. The proposed topology is shown in Figure 3-1 and it shows that the vehicle is entirely driven by electric motors. The power flows are indicated with thick directional dark lines while the communication and control connections are shown in dotted blue lines. The functional view of each component and how they are expected to interact and function are given below.

- **Trajectory Waypoint Planner:** This component uses Real-time kinematic

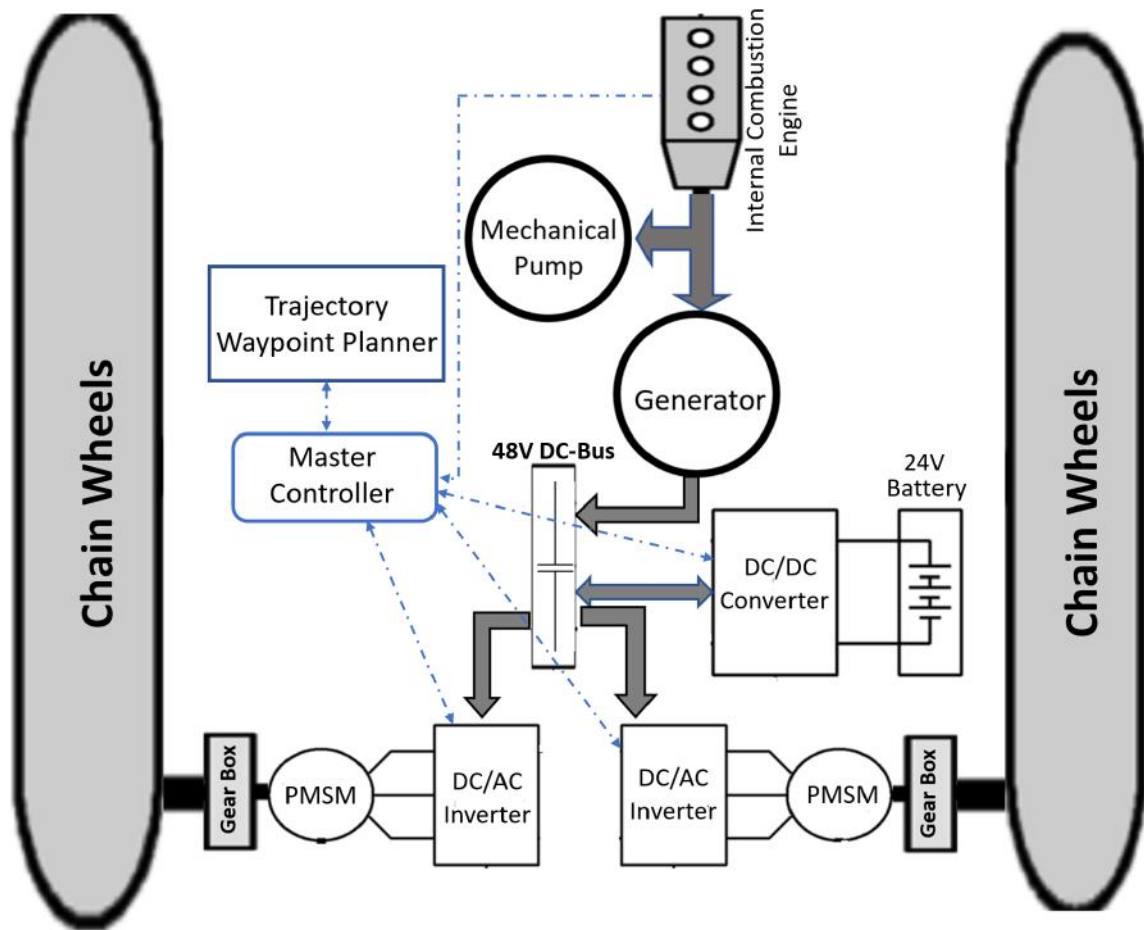


Figure 3-1: Proposed topology of series HEV

(RTK) positioning system for geolocation planning to map-out waypoints for the vehicle to follow through. This procedure is the backbone for autonomous vehicle capabilities.

- **Master Controller:** The master controller is the link between the electrical section with other parts of the vehicle and the external remote controller. The master controller also feels the conditions of the ICE to acknowledge the mechanical demands and apportion power limits to electrical load as necessary. The master controller also feels the battery and motors conditions via their respective converters.
- **Internal Combustion Engine (ICE):** The ICE serves as the primary energy source in the vehicle. The crank shaft of the engine is connected to both me-

chanical pump and the electric generator shafts. The ICE also communicates its speed and estimated power output with the master controller.

- **Mechanical Pump:** The pump is a hydraulic motor used to drive agricultural activity equipment such as the grass-cutter. The mechanical pump has higher priority against the generator as a recipient of ICE power.
- **Generator:** The generator is the main source of electrical energy in this topology. The generator mainly establishes and maintains a 48V dc-link bus system by charging and maintaining the charge on the dc-link capacitor. The generator does not directly supply power to other components such as the PMSM and battery.
- **DC-Link:** The dc-link is composed of the system capacitor which acts as an intermediary between the electrical sources (generator and battery) and the electrical load (PMSM). The capacitor helps to deliver instantaneous power to the motors when needed as capacitors have quite fast dynamics.
- **DC/DC Converter:** The dc/dc converter is a bidirectional boost converter that interfaces the battery into the entire system. It also serves to control the power flow into and from the dc-link. It can be regarded as the battery charger or charge controller. The dc/dc converter also communicates with the master controller for proper scheduling via its own local controller.
- **Battery:** The 24V battery is expected to function as a back-up or assistant in replenishing dc-link charge in cases where the generator cannot meet PMSM power demand due to allocation of more power to the mechanical pump.
- **DC/AC Inverter:** The inverter also has its own local controller which it uses to interact and receive commands from the master control as regards waypoints and trajectory information. It facilitates the implementations of the commands from current control by giving appropriate voltages to the motors. The local controller also receives rotor speed and phase current information from the motors to implement close loop controls.

- **Permanent Magnet Synchronous Motor (PMSM):** The PMSM is the only source of mechanical torque for driving the electric vehicle via the two wheel tracks. The motors see the entire mass of the vehicle as its load torque.
- **Gear box:** The gear box help in speed reduction and torque multiplication by a factor of the gear ratio, n , which in this application is 50:1. As the motor torque is ordinarily not enough to drive the vehicle but has a high speed that the vehicle does not need, the gear is therefore important.

3.2.1 System Design

It is expected that the proposed vehicle will be capable of mowing different thickness of heavy farm grass and scrubs, to function at different terrains and on both flat and mountainous landscapes ranging $[-60^\circ, 60^\circ]$ inclination angles. In light of limited resources, it is therefore paramount to properly assign design parameters for both mechanical power and electrical power components.

The mechanical scheme is connected in tandem to the ICE via the hydraulic pump which pumps hydraulic fluid based on pressure demand of the hydraulic motor. The pressure demand by the motor is dependent on the resistance to motion of the flail head depending on how thick the grass or bush in the landscape is. This is depicted in Figure 3-2 and the power required by the mechanical pump is given in (3.1).

$$P_{Mech} = P_{hyd} Q \quad (3.1)$$

where P_{Mech} is the mechanical power demanded by pump, P_{hyd} is the hydraulic pump pressure, and Q is the volumetric flow rate of the fluid.

The density or thickness of farm grass and speed of vehicle, V , will affect P_{hyd} and P_{Mech} . In a case of low or mild grass density, V has some tolerance to increase as P_{hyd} will be low. On the other hand, if the grass density is high, P_{hyd} and, hence, P_{Mech} will be high. Any attempt to increase V will further increase P_{hyd} and P_{Mech} accordingly. This translates to enormous consumption of the available ICE power, P_{ICE} . In this application $P_{ICE} = 18\text{kW}$, $Q = 50\text{Litres}/\text{min}$, while $P_{hyd} \in [100\text{bar}, 180\text{bar}]$ is ex-

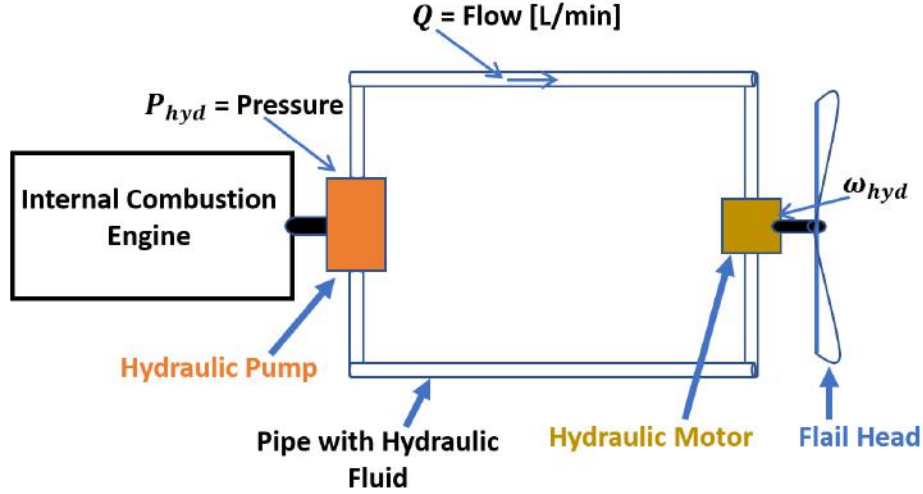


Figure 3-2: Mechanical hydraulic scheme

pected in the region landscape, $P_{hyd} = 160\text{bar}$. This gives $P_{Mech} \in [8.333\text{kW}, 15\text{kW}]$ which is about 46.3% - 83.33% of P_{ICE} . This intensive energy usage and the agricultural application makes the hydraulic demand a priority. On the other hand, it is the electrical power that moves the vehicle and determines velocity, hence, the question of if there will remain enough power to move on mountains of upto 60° is expected.

On the other hand, the electric motors dictate V of the entire vehicle and requires power. It is known that moving on an inclined terrain needs constant torque to fight against gravitational effects and additional power to accelerate, unlike moving on a flat surface that depends only on overcoming frictional forces. It is worthy of note that coefficient of friction, μ , used in this thesis are 0.05, 0.1 and 0.2 and are based on field factors. This scenario with the associated forces is shown in Figure 3-3. From the diagram, the forces required to move the vehicle on flat or inclined surfaces are given in (3.2).

$$F_d = Mg [\mu \cos \theta_{inc} + \sin \theta_{inc}] \quad (3.2)$$

where F_d is the driving force, M is mass of vehicle, g is acceleration due to gravity, μ is the coefficient of friction.

By exploring the expected range of θ_{inc} and values of μ in (3.2) using an estimated $M = 700\text{kg}$, it is seen that F_d varies $[343.35\text{N}, 1373.4\text{N}]$ on flat ground and has

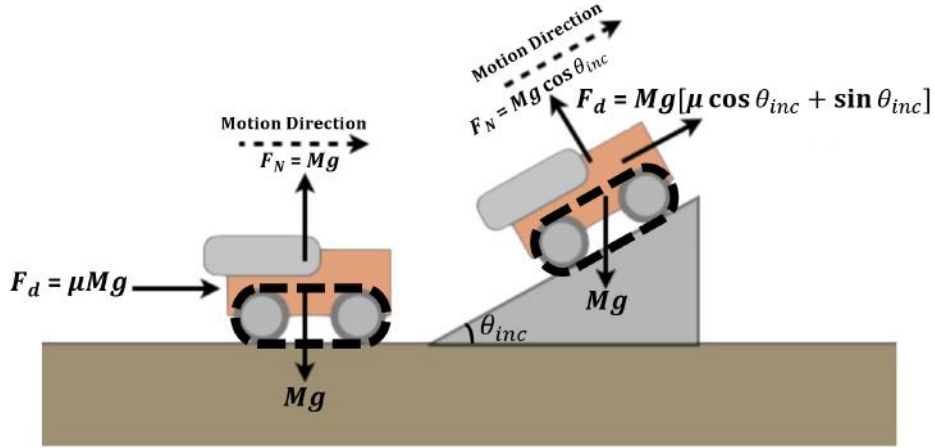


Figure 3-3: Forces required for vehicle motion

highest value of $F_d = 6633.70\text{N}$ at $\theta_{inc} = 60^\circ$ and $\mu = 0.2$, thus giving the maximum demand. More so, chain tracks will require wheel and rudders to support rolling, a wheel radius, $R \simeq 0.17\text{m}$, is expected, and maximum linear velocity estimated for the vehicle, $V_{max} = 1.96\text{m/s} \pm 0.15\text{m/s}$. As earlier stated the ICE power available for the generator, $P_{ICE-Gen}$ is limited to $3\text{kW} - 9.667\text{kW}$ based on the level of P_{Mech} . The most severe case at $F_d = 6633.70\text{N}$ for $\theta_{inc} = 60^\circ$ and $\mu = 0.2$ will require generator electrical power $P_{Gen} = 13\text{kW}$ to move at $V = 1.96\text{m/s}$, which is mutually exclusive with all levels of mechanical work. Hence, the only solution is to reduce the speed with elevation.

In order to size the electric motors, it is not practical to size at the limits of $P_{ICE-Gen}$, ie 3kW or 9.667kW , hence, an average of $P_{Mot} = 6.334\text{kW}$ is used as base, ie each motor is rated one-half of P_{Mot} . Since $P_{hyd} = 160\text{bar}$ at $P_{Mech} = 13.33\text{kW}$ is most common scenario and leaves just $P_{ICE-Gen} = 4.67\text{kW}$ for the generator, which is just 1.664kW shy from $P_{Mot} = 6.334\text{kW}$. This difference can be supplied by the inclusion of battery energy storage sized at about $P_{Bat} \simeq 1.7\text{kWh} - 2.2\text{kWh}$ for the machine to work at rated power if needed. At this rate, it is calculated that the speed of the wheels, ω_{wh} , at full motor power is limited $\omega_{wh} = 110\text{RPM}$ and only $P_{Gen} = 2.7\text{kW}$ as maximum demand on flat surface which is less than lower boundary of $P_{ICE-Gen}$ and needs no battery support. However, at higher inclinations the battery support may be needed depending on P_{Mech} , in the worst case of $F_d = 6633.70\text{N}$ at

$\theta_{inc} = 60^\circ$, a speed of 0.95m/s and $\omega_{wh} = 53.63\text{RPM}$ can be sustained at full motor power which will be lower for any condition that cannot guarantee full motor power.

Hence, motor ratings of approximately 3.1kW which will demand 66A at 48V dc-link aided by battery of size of about 2kWh, while the generator should be sized above $P_{Mot} = 6.334\text{kW}$ is proposed. To choose a motor to meet the specified ratings and that has a speed limit of 5500RPM as done in this thesis, will require a gear of gear-ratio 50:1 to maintain $\omega_{wh} = 110\text{RPM}$ on flat surfaces.

Analysis were carried out to show the effect of battery energy supply in improving productivity in smaller time. The battery can allow increasing vehicle speed and therefore the mileage with time. Four cases were studied; three cases at $\theta_{inc} = 15^\circ$ for $\mu = [0.05, 0.1, 0.2]$ and one case at $\theta_{inc} = 30^\circ$ for $\mu = 0.1$ were compared for the case of $P_{hyd} = 160\text{bar}$ at $P_{Mech} = 13.33\text{kW}$ and, hence, $P_{ICE-Gen} = 4.67\text{kW}$. The velocity profile for the vehicle and the state of charge of the battery as time progress are shown in Figures (3-4) and (3-5).

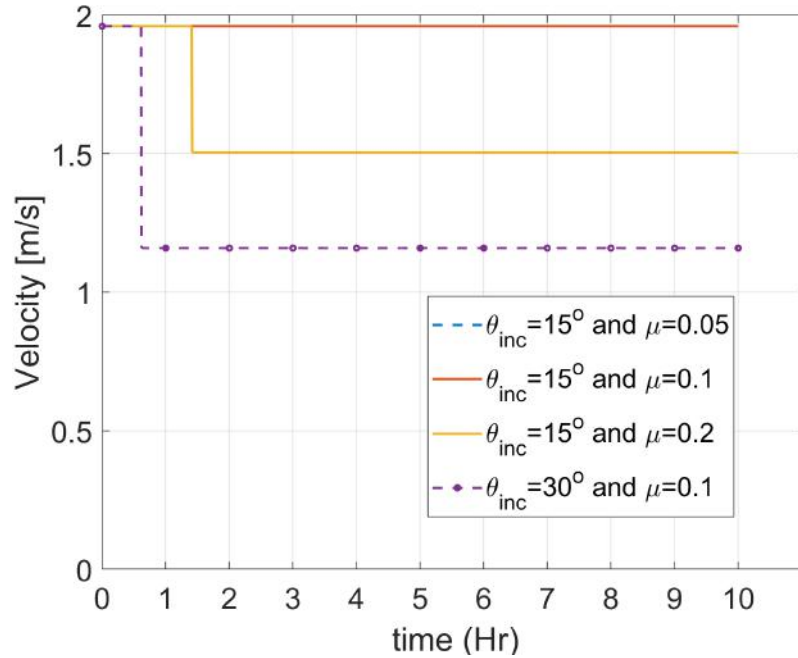


Figure 3-4: Velocity profile of the vehicle at different landscapes

It is seen that $\theta_{inc} = 15^\circ$ for $\mu = 0.05$ does not require battery support, that $\theta_{inc} = 15^\circ$ for $\mu = 0.1$ requires little battery support and would take above 10 hours

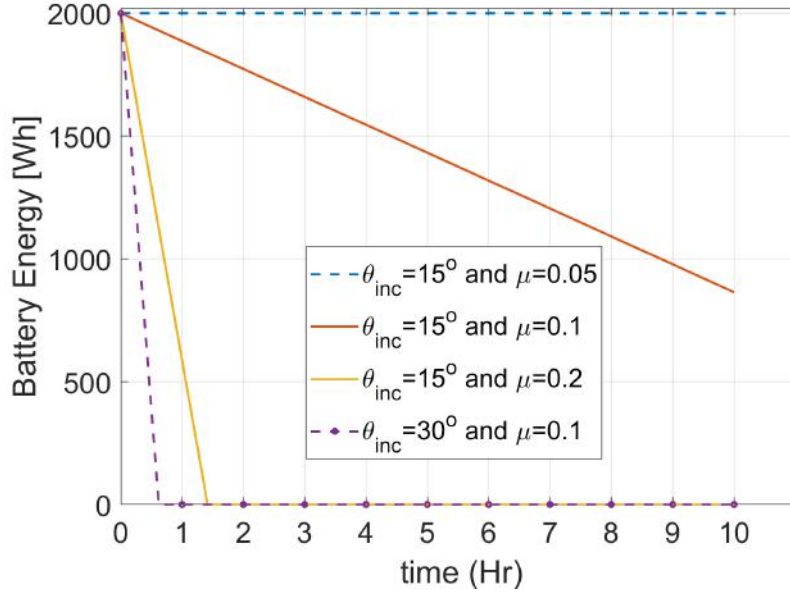


Figure 3-5: The state of charge of battery as it discharges into PMSM

of full load work and speed to deplete the battery of 2kWh. However, it is seen that at higher frictional force at $\theta_{inc} = 15^\circ$ for $\mu = 0.2$ and higher inclination $\theta_{inc} = 30^\circ$ for $\mu = 0.1$, the battery is quickly drained and as fast as less than 1 hour in the latter case, thereby limiting speed to the limits provided by $P_{ICE-Gen}$.

3.3 Energy Management System

The Energy Management System (EMS) of the HEV entails how to apportion the ICE energy output between mechanical pneumatic pumps and the electric motors. It also details when the batteries can be discharged into the motors or charged by the generator as necessary. The scheme is illustrated in (3.3-3.6) and shown in Figure 3-6. The EMS scheme ranks the mechanical pump above the generator for ICE power output which is ensured by (3.3) where $P_{ICE-Gen}$, the ICE power available for the generator, is the remnant after the mechanical pump demand is satisfied. Afterward there are two cases; Case I demands support from the batteries to service the motors, while Case II depicts moments of less mechanical and motor demands which enables possible charging of the batteries.

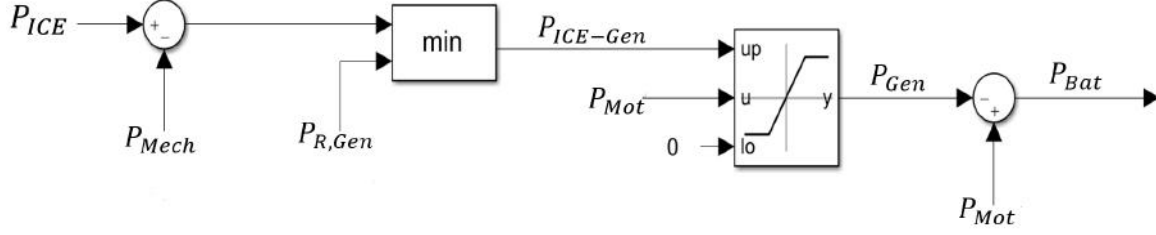


Figure 3-6: Energy Management Scheme for the HEV

$$P_{ICE-Gen} = \min[P_{ICE} - P_{Mech}, P_{R,Gen}] \quad (3.3)$$

Case I: if $P_{Mot} > P_{ICE-Gen}$;

$$P_{Gen} = P_{ICE-Gen} \quad (3.4)$$

$$P_{Mot} = P_{Gen} + P_{Bat} \quad (3.5)$$

Case II: if $P_{Mot} < P_{ICE-Gen}$;

$$P_{Mot} = P_{Gen} \quad (3.6)$$

where P_{ICE} is the power output of the ICE, P_{Mech} is the mechanical power demand, $P_{ICE-Gen}$ is the portion of ICE power output available for the generator, $P_{R,Gen}$ is the rated size of the generator, P_{Gen} is the actual generator output, P_{Mot} is the total power demand from the motors, and P_{Bat} is the power flow from the battery.

3.4 Battery Charge Controller

The point of connection of the Battery to the energy system is via the dc link connected to the batteries via bidirectional dc-dc boost converter. The bidirectional dc-dc boost converter has the capability to boost in a direction and buck in another direction of power flow and it is popularly used with batteries in electric vehicle applications [25]. In this application, it is expected that the battery is at lower voltage than the dc link and the proposed topology uses two batteries and is given in Figure 3-7. It is expected that the two batteries operate as a single unit as seen at the dc-link and entire EMS, hence the total battery current is defined in (3.7). The two parallel boost converters are entirely symmetrical, therefore, their operation as a single unit

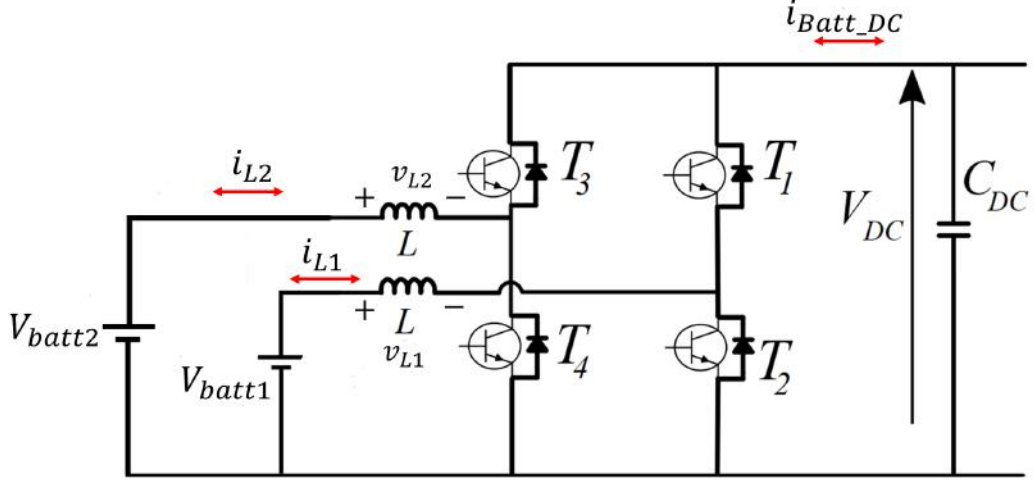


Figure 3-7: Bidirectional boost converter topology

is detailed in section 3.4.1.

$$i_{Batt} = i_{L1} + i_{L2} \quad (3.7)$$

where i_{Batt} is the entire battery current, i_{L1} and i_{L2} are the individual battery currents.

3.4.1 Operation of Bidirectional DC-DC Boost Converter

The bidirectional dc-dc boost converter will work as boost converter when discharging the batteries into the dc-link and as a buck converter when charging the battery from the dc-link. As a single unit having just transistors T_1 and T_2 , the converter shown in Figure 3-8 depicts the working procedures of bidirectional boost converter working in the boost mode. In this boost mode, the duty ratio of the converter is defined by the operation of transistor T_1 and the two transistor work in a complementary function. As shown in Figure 3-8, when transistor T_1 is on, the inductor current, i_L , flows entirely via T_1 while the dc-link supplies the load, hence, discharging the dc-link. During this interval, the inductor field is charged and $v_L = V_{Batt}$. In the second interval, transistor T_1 is off while transistor T_2 is on, but its the body diode of T_2 that conducts the inductor current in this mode. In this interval, $v_L = V_{Batt} - V_{DC}$, the magnetic field of the inductor discharges into the dc-link, thereby, charging the dc-link. By noting that the first interval take a fraction, D , of the switching period, T_s , and that the average voltage across an inductor in a cycle is zero, equation (3.8)

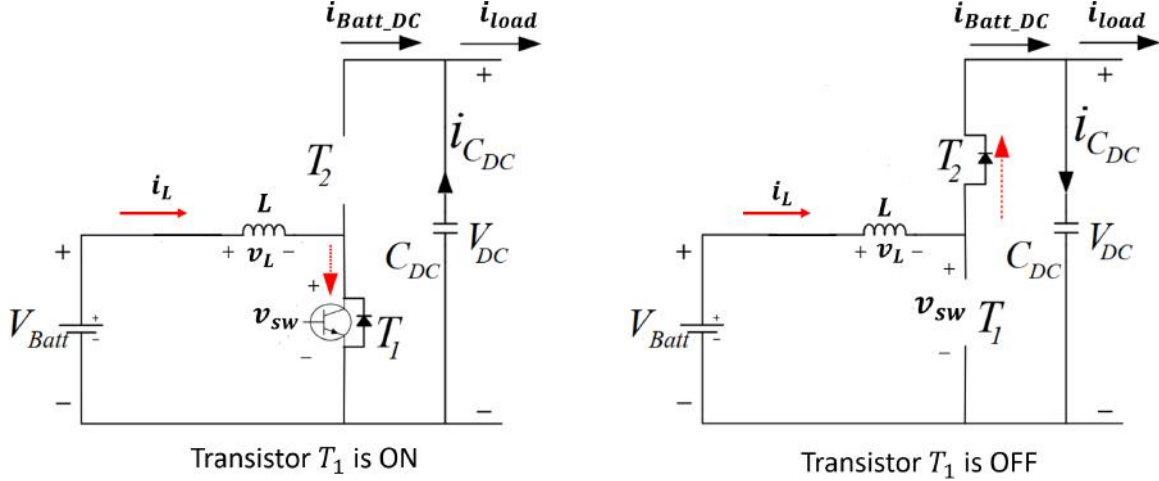


Figure 3-8: Working of bidirectional boost converter in boost mode

can be written for v_L .

$$\langle v_L \rangle = \int_0^{DT_s} V_{Batt} dt + \int_{DT_s}^{T_s} V_{Batt} - V_{DC} dt = 0 \quad (3.8)$$

where v_L is voltage drop across inductor, D is duty ratio, T_s is switching period of transistor, V_{DC} is dc-link voltage, V_{Batt} is the battery voltage.

In the above expression for average inductor voltage, only steady-state conditions and inductor volts-seconds balance are assumed. Furthermore, solving (3.8) gives the required duty ratio to maintain the expected V_{DC} as given in (3.9).

$$V_{DC} = \frac{V_{Batt}}{1 - D} \quad (3.9)$$

On the otherhand, for the bidirectional boost converter to reverse power flow and charge the batteries from dc-link, it operates in the buck mode. The buck mode of operation is illustrated in Figure 3-9. In this mode, the duty ratio is defined by transistor T_2 . In the first interval of the switching period, T_2 is on and conducts current to the battery while T_1 is off. In this period, $v_L = V_{DC} - V_{Batt}$. In the second interval, the diode of transistor T_1 conducts the current in the loop containing V_{Batt} , T_1 and the inductor, while T_2 is open. In this interval, $v_L = -V_{Batt}$. And again, by using the inductor volts-seconds balance, assuming steady state conditions, neglecting

inductor current ripples and using the fact that average voltage across an inductor is zero in a cycle, equation (3.10) can be written for inductor voltage v_L [26].

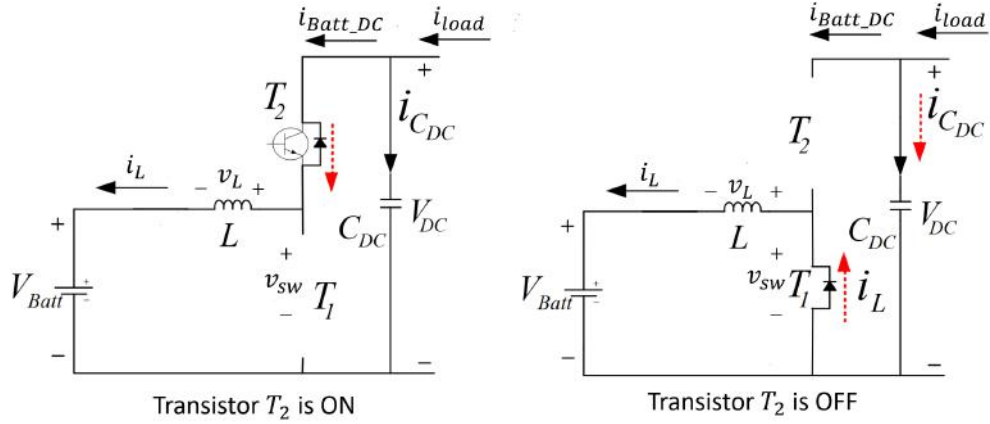


Figure 3-9: Working of bidirectional boost converter in buck mode

$$\langle v_L \rangle = \int_0^{DT_s} V_{DC} - V_{Batt} dt - \int_{DT_s}^{T_s} V_{Batt} dt = 0 \quad (3.10)$$

Solving the above equation, gives the relationship between V_{DC} and V_{Batt} required to maintain both voltages via the required duty cycle of the switch T_2 . This expression is given in (3.11).

$$V_{DC} = \frac{1}{D} V_{Batt} \quad (3.11)$$

3.4.2 Average Model of Bidirectional DC-DC Boost Converter

The model of bidirectional dc-dc boost converter described in subsection 3.4.1 contains elements, such as inductor and capacitor, which makes the entire dynamics of the system more complex and less suitable for EMS planning purposes because long simulation times will be required to solve the systems. For this purpose, the average model of the bidirectional boost converter is used. Although the model removes the effects of the dynamics of the inductor and capacitor, several loss elements are taken into consideration. The loss elements are the resistances of the inductor and transistor, and the on-voltage drop of the diode and the transistor when in conduction as

shown in Figure 3-10.

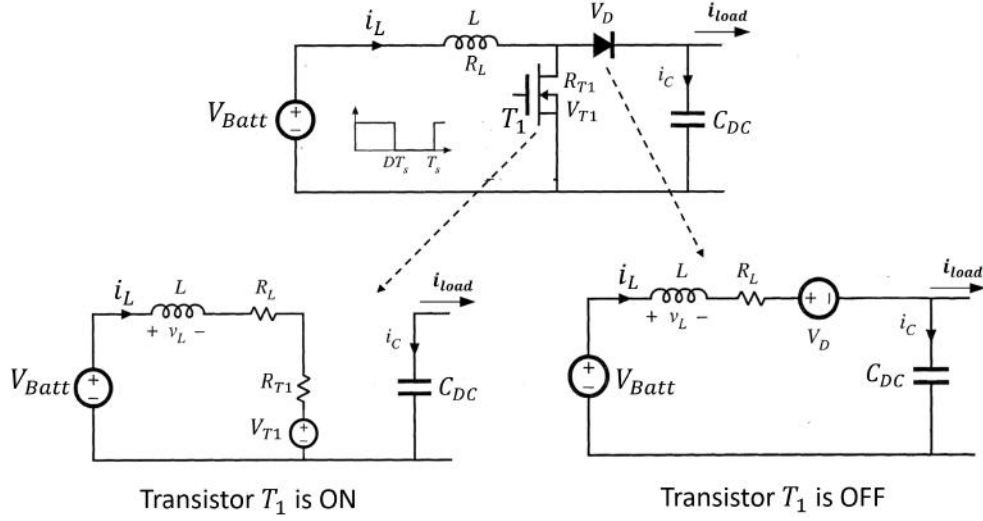


Figure 3-10: Operating cycle of average model of bidirectional boost converter

Figure 3-10 shows the two states of the bidirectional boost converter when either transistor is conducting and the effects of the loss elements are evident. This changes the values of the voltage across the inductor and the current through the capacitor when the transistor T_1 is on and off, which are given in (3.12) and (3.13) respectively.

$$v_L = \begin{cases} V_{Batt} - i_L (R_L + R_{T1}) - V_{T1}, & \text{When } T_1 \text{ is ON} \\ V_{Batt} - i_L R_L - V_D - V_{DC}, & \text{When } T_1 \text{ is OFF} \end{cases} \quad (3.12)$$

where i_L is the inductor current, R_L and R_{T1} are the resistance of inductor and on resistor of the transistor T_1 , V_{T1} is the on voltage of transistor T_1 , and V_D is diode on voltage.

$$i_C = \begin{cases} -i_{load}, & \text{When } T_1 \text{ is ON} \\ i_L - i_{load}, & \text{When } T_1 \text{ is OFF} \end{cases} \quad (3.13)$$

where i_C is capacitor current, and i_{load} is the load current.

By further assuming steady-state conditions and neglecting ripples in inductor current, therefore replacing i_L with I_L to represent average inductor current, and similar conditions for capacitor voltage ripples, then average values of v_L and i_C can

be found. The inductor volts-seconds balance and capacitor charge balance equations are written in (3.14) and (3.15) respectively.

$$\langle v_L \rangle = \int_0^{DT_s} V_{Batt} - I_L (R_L + R_{T1}) - V_{T1} dt + \int_{DT_s}^{T_s} V_{Batt} - I_L R_L - V_D - V_{DC} dt = 0 \quad (3.14)$$

$$\langle i_C \rangle = \int_0^{DT_s} -i_{load} dt - \int_{DT_s}^{T_s} I_L - i_{load} dt = 0 \quad (3.15)$$

By solving these equations, summing each to zero on the RHS conforming the two to be in the form of Kirchhoff's voltage and current laws, and letting $D' = 1 - D$ gives (3.16) and (3.17). Using these equations in the present form, the average equivalent circuit of the bidirectional dc-dc boost converter can be obtained and shown in Figure 3-11. The average equivalent circuit is made of two circuits coupled via the average inductor current, I_L , and dc-link voltage, V_{DC} via dependent current and voltage sources. Also, the on-voltages of the diode and transistor are replaced with duty-cycle dependent voltage sources depicting their conduction periods and amount of impact. This model is used henceforth for simulation due to shorter simulation time and convenience.

$$V_{Batt} - I_L (R_L + DR_{T1}) - (D'V_D + DV_{T1}) - D'V_{DC} = 0 \quad (3.16)$$

$$D'I_L - i_{load} = 0 \quad (3.17)$$

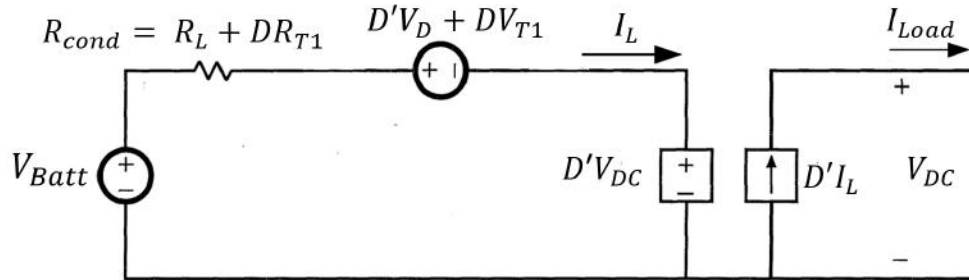


Figure 3-11: Average model of bidirectional boost converter [26]

3.4.3 Battery Current Controller Design

The amount of power the battery supplies or consumes needs to be regulated in order to avoid irregular and unexpected behaviours from the battery and the entire system. In order to design the battery power controller, the output current of the battery which is basically the inductor current, i_L is to be controlled. In order to control i_L , then v_L must be controllable. This can be done by controlling the switching or duty cycle of the transistors. Hence, as shown in Figure 3-7, the loop containing battery, inductor and transistor T_1 gives loop voltage equation given in (3.18). And knowing that the average voltage across transistor T_1 in the entire cycle is a fraction of V_{DC} given as $v_{sw} = V_{DC}(1 - D)$, then (3.18) can be solved for the required duty-cycle, D , to maintain a commanded voltage across the inductor for current control. This duty cycle is given in (3.19).

$$v_L = V_{Batt} - v_{sw} \quad \text{But : } v_{sw} = V_{DC}(1 - D) \quad (3.18)$$

$$D = \frac{v_L - V_{Batt}}{V_{DC}} + 1 \quad (3.19)$$

Hence, the inductor is the plant of the control system, and using just the inductor internal resistance and neglecting the transistor resistance, $R_{T1} \ll R_L$, the transfer function for the system is given in (3.20), while the transfer function of the controller, proportional integral (PI), is given in (3.21). By using the popular pole-zero cancellation technique, the controller constants are obtained and given in (3.22) and (3.23). The controller scheme is shown in Figure 3-12.

$$TF_L = \frac{1}{Ls + R_L} \quad (3.20)$$

$$TF_{PI} = K_P \frac{s + K_I}{s} \quad (3.21)$$

$$K_{P,Batt}^i = 2\pi f_{c,Batt}^i L \quad (3.22)$$

$$K_{I,Batt}^i = \frac{R_L}{L} \quad (3.23)$$

where $K_{P,Batt}^i$, $K_{I,Batt}^i$ and $f_{c,Batt}^i$ are PI proportional and integral term for the battery current controller, and the cut-off or bandwidth of the battery current control loop.

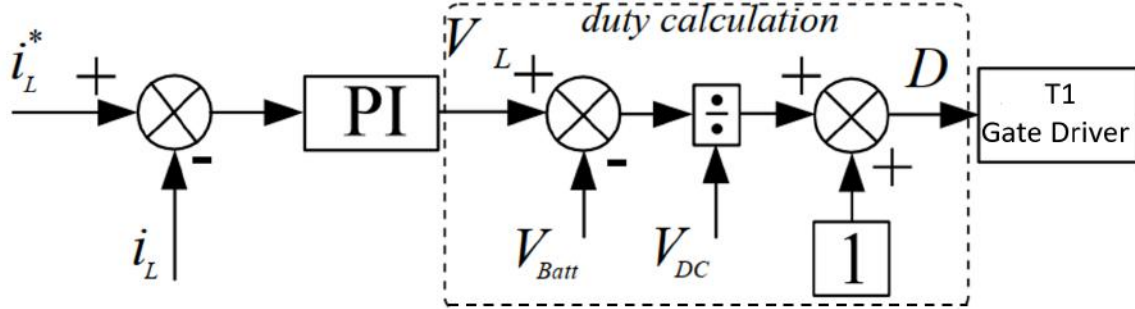


Figure 3-12: Battery current control loop scheme

3.5 Energy Management Simulations

In this section simulations will be made based on the theories delineated in this chapter. The EMS plan will be exploited as earlier expounded; the ICE will be primary source of energy, mechanical load will have higher priority over the electric generator for power consumption. The electric motors are lumped as active power load, while the batteries will support the motors when needed.

Case I: Electric Motor at Rest Demands Zero Power

First a simulation at zero demand from the electric motor load was carried out. The Power ratings of the ICE, generator and power demand by the mechanical pump are shown in Figure 3-13 while the limits of the generator is given in Figure 3-14. It is seen in Figure 3-14 that at time $< 0.5sec$, the generator output power limit is constrained by its own rated size inspite of the available ICE power. But as the mechanical power rises, the generator output limit is then constrained by the availability of ICE power. In this case the power output of the generator is zero, and the battery too is zero as shown in Figure 3-14.

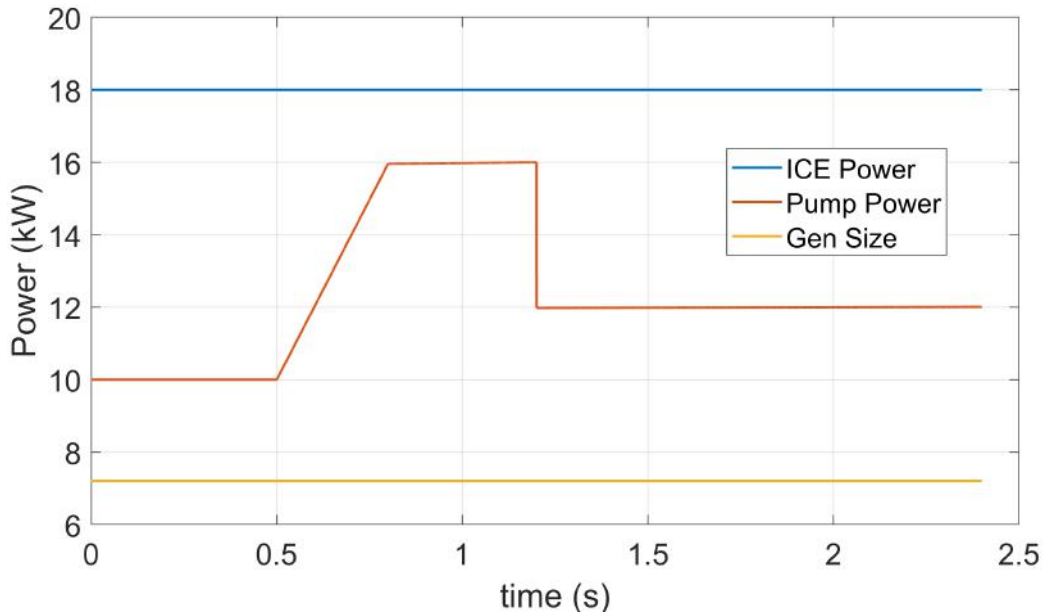


Figure 3-13: Power Ratings of primary equipment

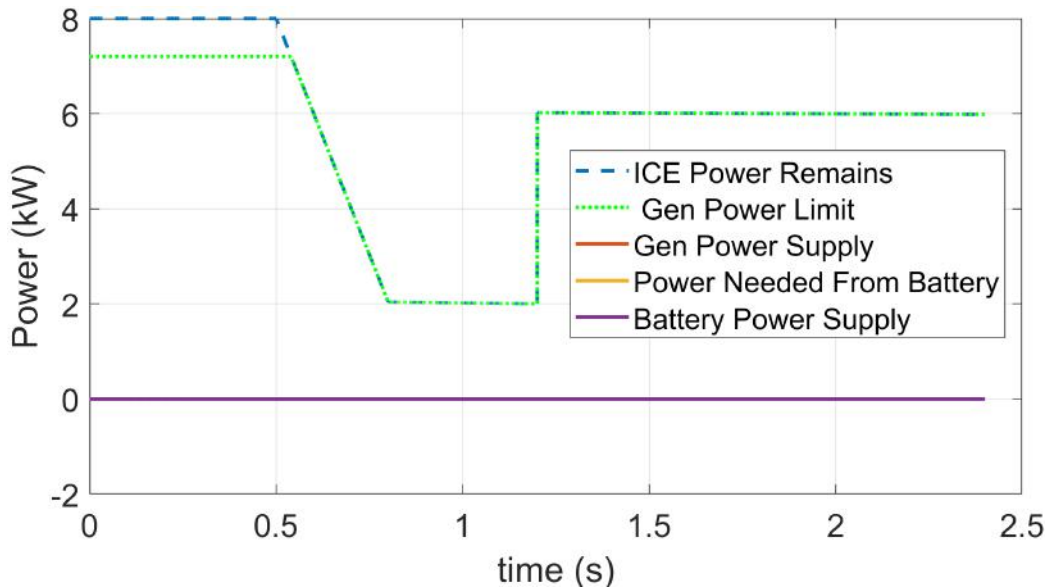


Figure 3-14: Generator power limits and, Generator and Battery power at no motor load

Case II: Electric Motor with Three Instances of Step Power Demand

In this case, several step increases of motor power demand was simulated via the motors speed control loop. In this case the generator response to these spikes of demands is shown in Figure 3-15. It is seen that the Generator does not exceed its

power limits with time, and at about 0.8sec, it hits the limit which made the battery to respond. It is further shown in Figure 3-16 that the summation of both the generator and batteries output powers cover the motor power demands for the most part. In spot time of massive spikes, the capacitor of dc-link supplies this current in which the batteries are slow to replace, thereby, causing reductions in dc-link voltage values.

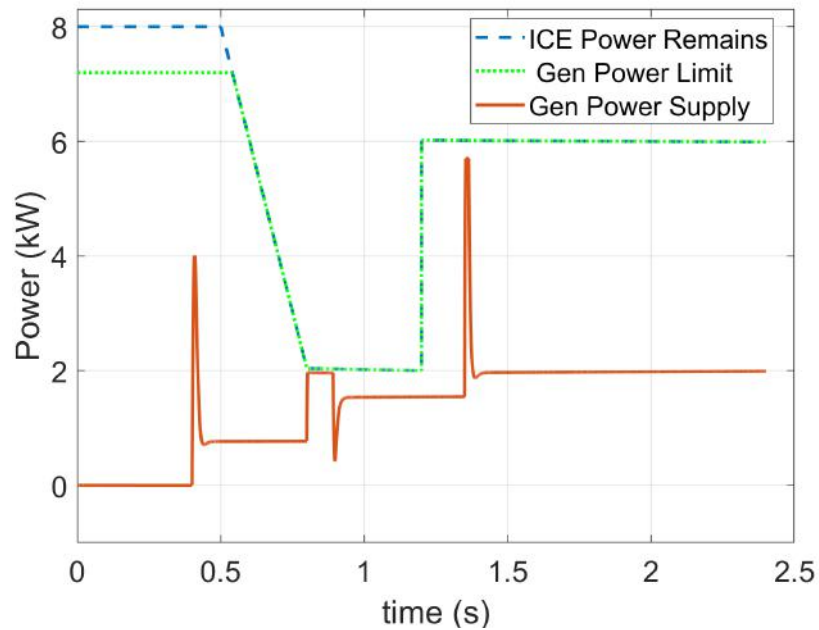


Figure 3-15: Generator power limits and power output with motor-power demand

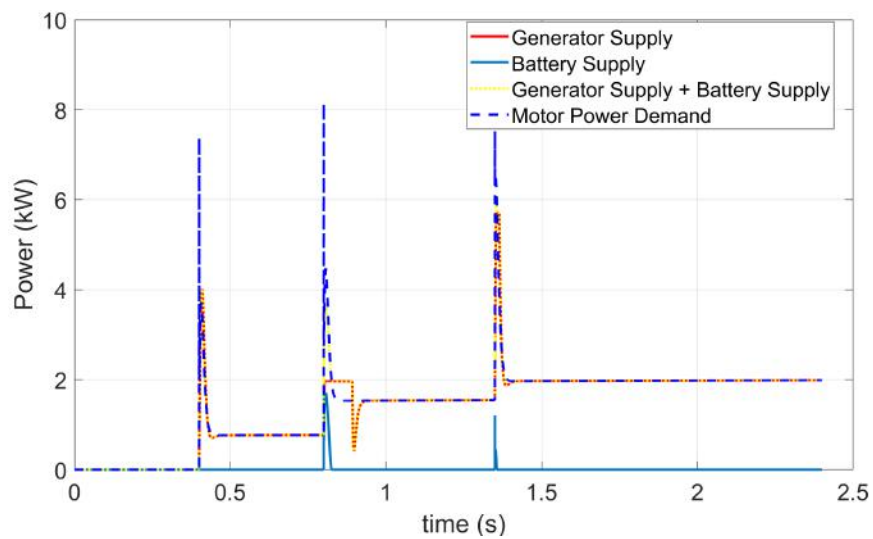


Figure 3-16: Generator and battery power meeting motor-power demand

In this scenario, the motor draws power from the dc-link, thereby causing a dip in dc-link voltage. The generator's voltage control mechanism responds to this voltage dip, by increasing its current output within the limits of the EMS. But motor step demands causes huge inrush currents, which requires the battery to help. Figure 3-17 shows the effects of the dynamics on dc-link voltage while Figure 3-18 shows the interactions of currents at the juncture of the dc-link. It is seen that the generator's current does not surpass its limits, and the battery supplies current only when motor demand passes the limits of available generator power. It is also worthy of note in Figure 3-18 that, although, the generator's current limit varies despite that the generator power limit is constant, such as in the intervals $0.8\text{sec} < t < 1.0\text{sec}$. This is because the currents in Figure 3-18 are plotted as seen at the dc-link node, hence, as the dc-link voltage varies the current directly varies with constant power. This is in contrast to the same generator current limits as seen from generator terminal which is depicted in Figure 3-19.

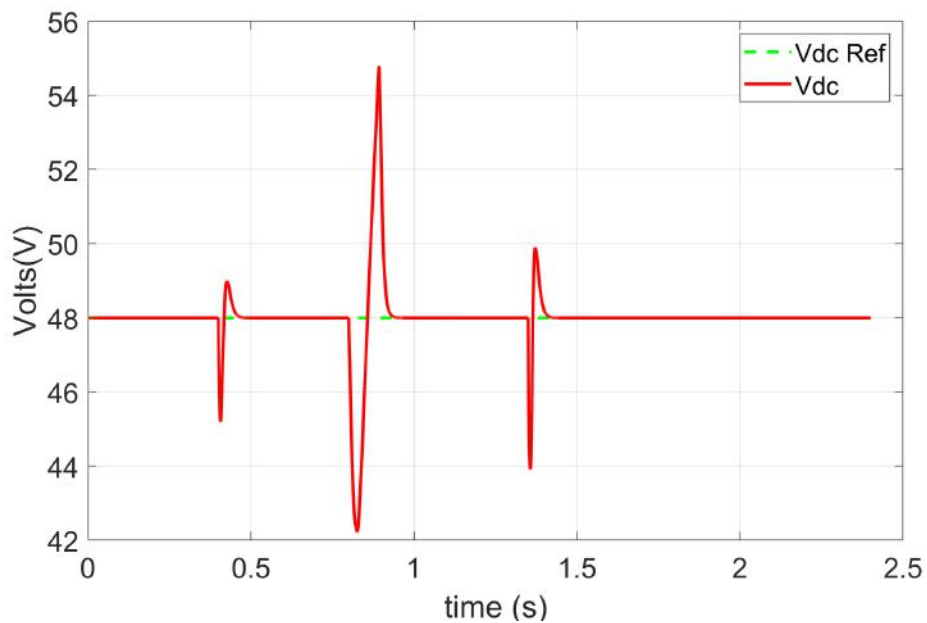


Figure 3-17: DC-Link voltage response during motor-power demand

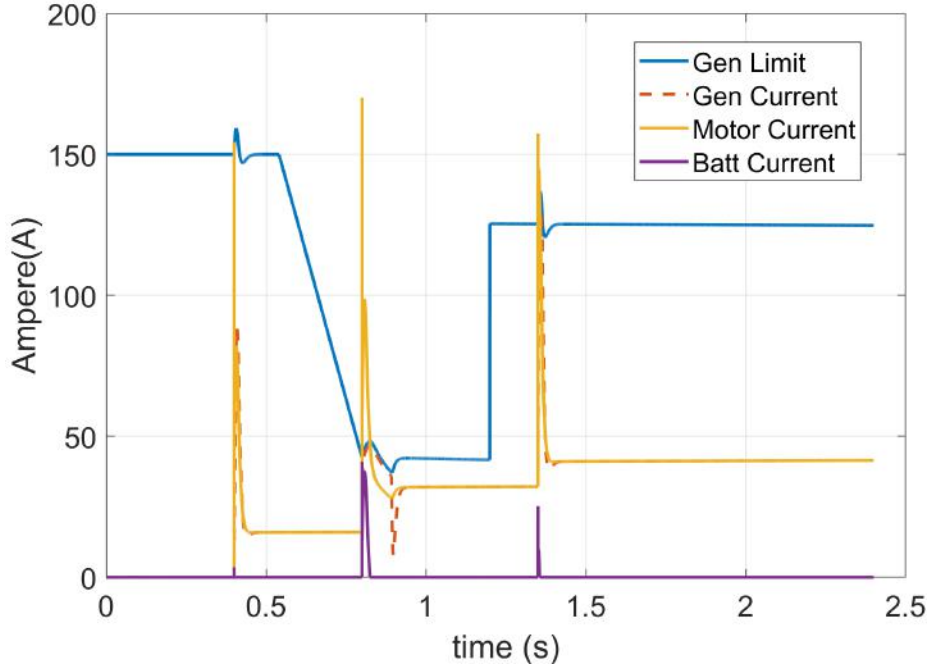


Figure 3-18: Currents at dc-link node during motor-power demand

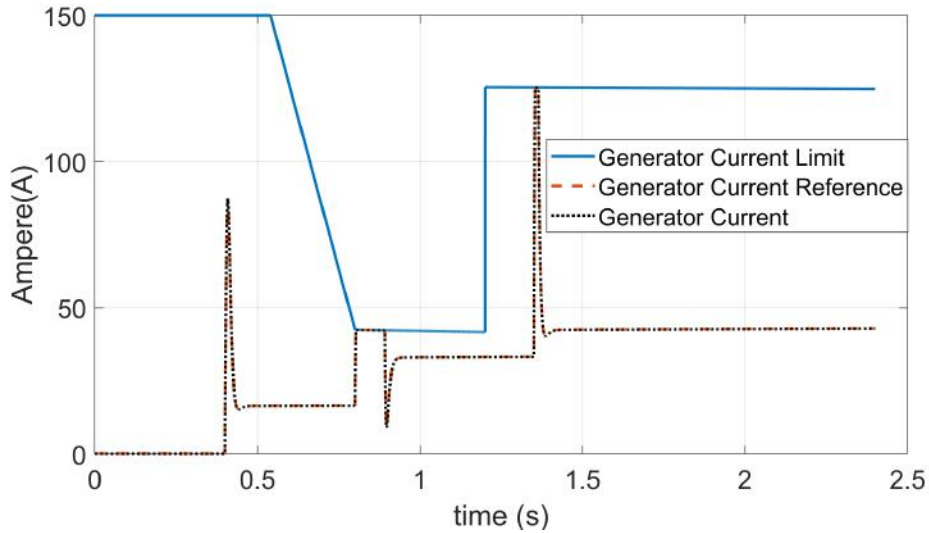


Figure 3-19: Generator currents at generator terminal

The battery behaviour in this case is depicted in Figure 3-20 which shows the power demanded from the battery along side the actual power delivered by the battery. More so, Figure 3-21 shows the inductor current reference and actual values as the battery responds to EMS demand for battery power. In Figure 3-20, it is seen at $t = 0.8\text{sec}$ that the EMS demands a huge power surge of 6kW from the battery, but

the battery only meets 2kW of this demand, this is because the batteries dynamics has much smaller bandwidth and is not as fast as the capacitor which supplies such surge demands. More so, the EMS, as earlier explained, does not factor in the presence of the dc-link capacitor as a source of such surge power. The response of the battery and generator has been possible due to the real-time modulation of the duty-cycle of their transistor switching patterns, these duty cycles are shown in Figure 3-22.

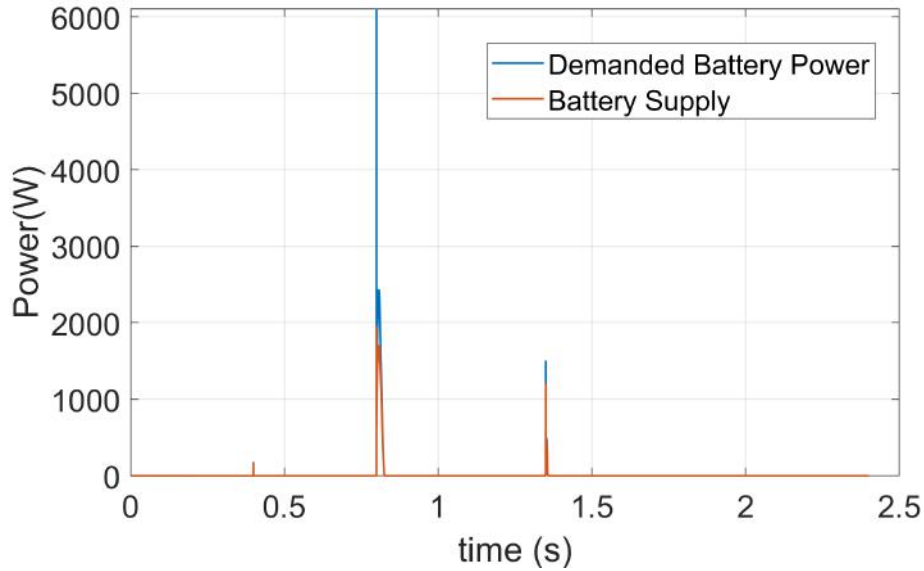


Figure 3-20: Battery power output and reference

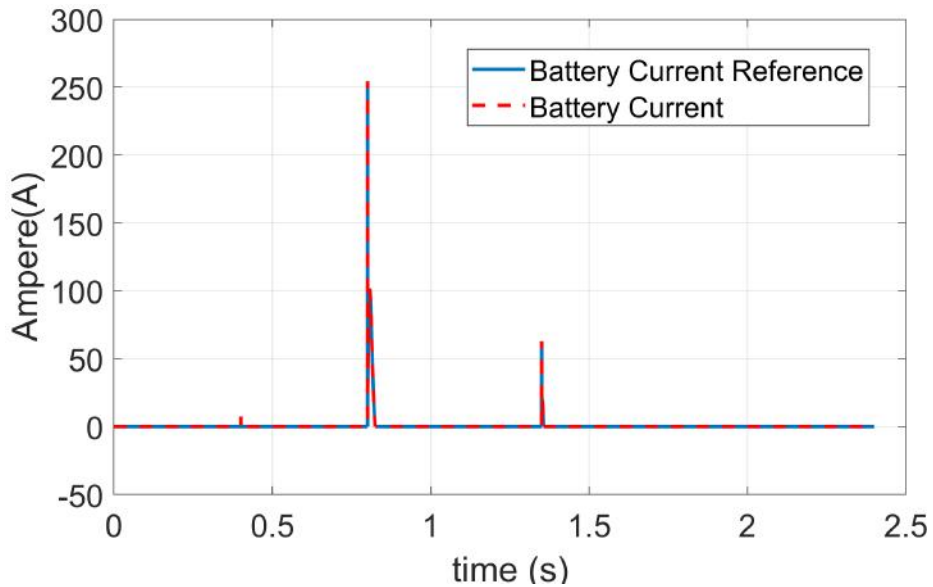


Figure 3-21: Battery Current output and reference at battery terminal

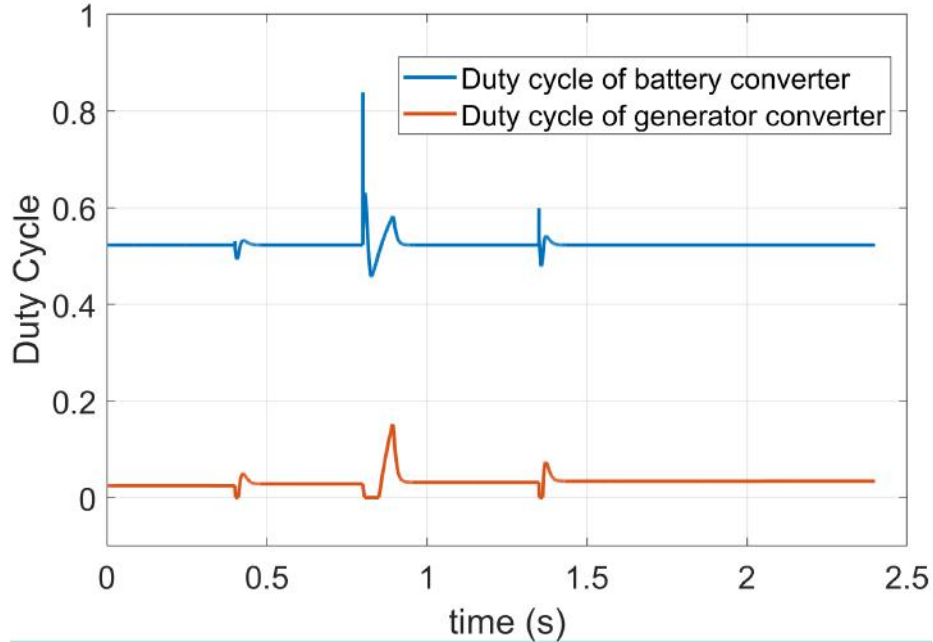


Figure 3-22: Duty cycle of battery and generator converters

3.6 Conclusion

This chapter has shown that energy management is essential in schemes of several energy and energy components. The chapters has also successfully shown that with proper energy management scheme, it is possible to efficiently run an energy intensive system without over-sizing of components. The inclusion of batteries can be a source of increased productivity in an intermittently mechanical-power intensive agricultural field. The scheme is also open to further improvement such as detailing the capacitor itself as a source of instantaneous power.

Chapter 4

Differential Drive Vehicle Analysis and Trajectory Control

4.1 Introduction

As earlier stated, the proposed vehicle topology employs motor to drive each wheel. These two PMSMs are driven independently which are said to be differentially driven since each motor speed is independent of the other but is controlled based on intended direction of motion. This chapters details the differential-drive vehicle dynamics and kinematics, but only after discussing the modeling of the utilized PMSM.

4.2 Differential Drive Kinematics

The kinematics of two-wheel driven vehicles explores the relationships among the quantities of motion of the entire vehicle with the quantities of the elements of the vehicle, such as speed and displacement, without factoring in the force that causes motion. As shown in Figure 4-1, using an instantaneous centre of curvature (ICC) and mapping out circular paths formed by each wheel gives (4.1) and (4.2) about radius at the instantaneous centre of curvature, R_{ICC} .

$$\omega(R_{icc} + \frac{D}{2}) = V_r \quad (4.1)$$

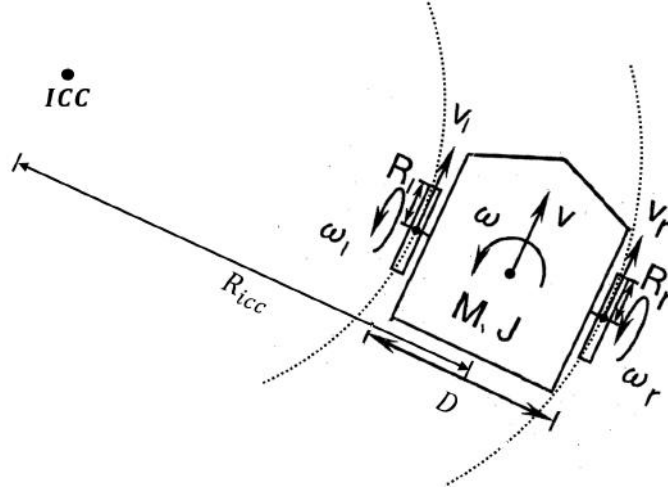


Figure 4-1: Vehicle kinematics parameters with ICC[27]

$$\omega(R_{icc} - \frac{D}{2}) = V_l \quad (4.2)$$

where ω is vehicle rotational speed, V_r and V_l is linear velocity of right and left wheels, D is width of the vehicle.

By solving the equations simultaneously and realizing that $V_r = \omega_r R_r$, $V_l = \omega_l R_l$, and $V = \omega R_{icc}$, the forward and inverse steering system kinematics models between the vehicle linear and rotational speeds, and those of the wheels, and R_{icc} , are obtained as in (4.3) - (4.5) [27, 28, 29] respectively.

$$\begin{bmatrix} V \\ \omega \end{bmatrix} = \begin{bmatrix} \frac{R_r}{2} & \frac{R_l}{2} \\ \frac{R_r}{D} & -\frac{R_l}{D} \end{bmatrix} \begin{bmatrix} \omega_r \\ \omega_l \end{bmatrix} \quad (4.3)$$

$$\begin{bmatrix} \omega_r \\ \omega_l \end{bmatrix} = \begin{bmatrix} \frac{1}{R_r} & \frac{D}{2R_r} \\ \frac{1}{R_l} & -\frac{D}{2R_l} \end{bmatrix} \begin{bmatrix} V \\ \omega \end{bmatrix} \quad (4.4)$$

$$R_{icc} = \frac{D V_r + V_l}{2 V_r - V_l} \quad (4.5)$$

where V is the linear velocity of the vehicle, R_r and R_l are radius of right and left wheel.

In order to obtain the present state of the vehicle, i.e (x, y, θ) , the real-time linear

and rotational velocities of the vehicle are projected to the front-side coordinates, which are further projected onto the global coordinates and summed in time [27],[30]. Figure 4-2 shows the vehicle in these two coordinates. It is obvious to realize that $V(t)$ has no component in the Y_{FS} direction which makes a non-holonomic system. Hence, the system present states in global coordinates or vehicle kinematics are given in (4.6)-(4.8) [31, 27, 28].

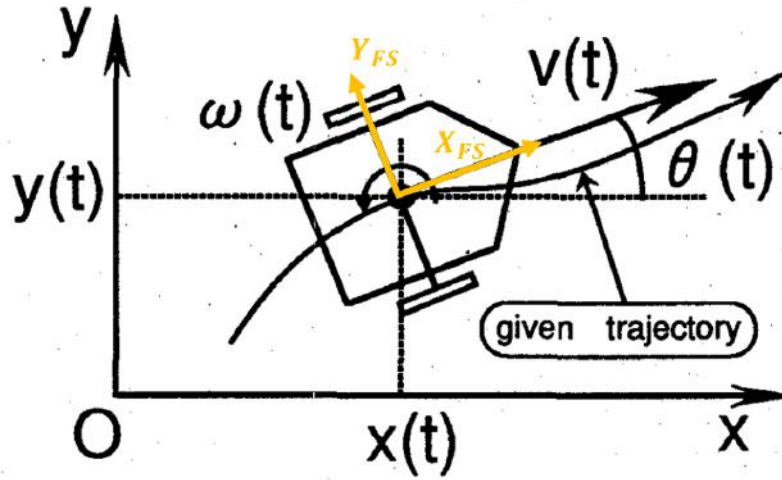


Figure 4-2: Vehicle front-side and global coordinates parameters [27, 30]

$$x(t) = \int_0^t V(\tau) \cos \theta d\tau \quad (4.6)$$

$$y(t) = \int_0^t V(\tau) \sin \theta d\tau \quad (4.7)$$

$$\theta(t) = \int_0^t \omega(\tau) d\tau \quad (4.8)$$

4.3 Vehicle Dynamics

Dynamics of the entire vehicle which considers and combines both the physical mass of the vehicle as shown in Figure 4-1 and the dynamics between the wheel and electric motors and there inter-connectivity is detailed herein. The parameters connecting the wheels, gears and electric motors are shown in Figure 4-3 [27].

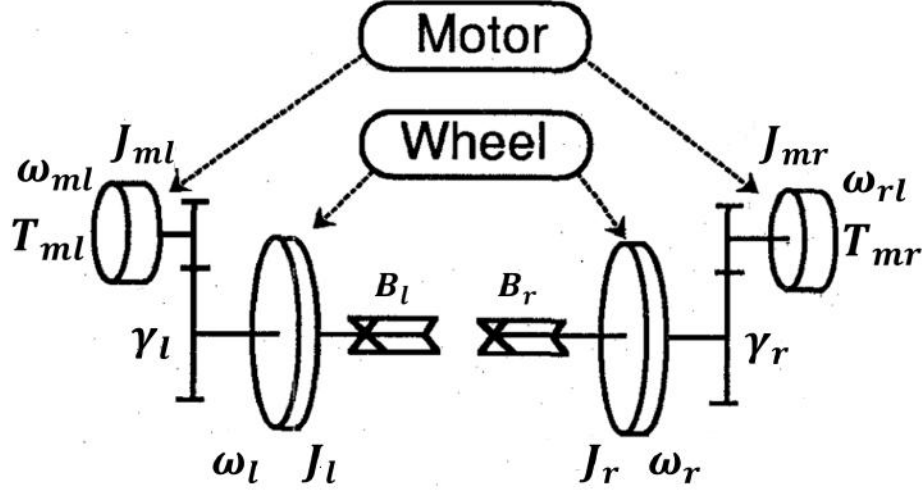


Figure 4-3: Parameters for wheel and motor dynamics in a dual-motor driven vehicle [27]

In exploiting dynamics, newtons laws are used for analyzing the forces required for linear and rotational of the entire vehicle as a lumped body of mass, which is then connected to the newtons law's analysis of the ability of the electric motors to drive the load torque connected to motors via wheels and gears. The summation of forces required for forward movement and anti-clockwise rotation of vehicle are given in (4.9) and (4.10) [27, 29].

$$f_r + f_l = M \frac{dV}{dt} \quad (4.9)$$

$$D(f_r - f_l) = J \frac{d\omega}{dt} \quad (4.10)$$

where f_r and f_l are right and left wheel force, M is mass of vehicle, J is moment for inertia of the vehicle.

By solving (4.9) - (4.10) simultaneously for the left and right wheel forces, and substituting the kinematics of (4.3), the two wheel forces required to move the vehicle are therefore obtained as given in (4.11) and (4.12) [27, 28, 29].

$$f_r = \frac{1}{2} \left[R_r \left(\frac{M}{2} + \frac{J}{D^2} \frac{\omega_r}{dt} \right) + R_l \left(\frac{M}{2} - \frac{J}{D^2} \frac{\omega_l}{dt} \right) \right] \quad (4.11)$$

$$f_l = \frac{1}{2} \left[R_r \left(\frac{M}{2} - \frac{J}{D^2} \frac{\omega_r}{dt} \right) + R_l \left(\frac{M}{2} + \frac{J}{D^2} \frac{\omega_l}{dt} \right) \right] \quad (4.12)$$

It is obvious that the wheel forces are coupled during angular acceleration of each wheel. Furthermore, from Figure 4-3 the transformations of load torques from wheels to motors leads required motor torques in (4.13) and (4.14) [27, 29]. The gear ratios are defined in (4.15).

$$T_{mr} = J_{mr} \frac{d\omega_{mr}}{dt} + \frac{1}{\gamma_r} [J_r \frac{d\omega_r}{dt} + B_r \omega_r + R_r f_r] \quad (4.13)$$

$$T_{ml} = J_{ml} \frac{d\omega_{ml}}{dt} + \frac{1}{\gamma_l} [J_l \frac{d\omega_l}{dt} + B_l \omega_l + R_l f_l] \quad (4.14)$$

$$\gamma_l = \frac{\omega_{ml}}{\omega_l} \quad \text{and} \quad \gamma_r = \frac{\omega_{mr}}{\omega_r} \quad (4.15)$$

where T_{mr} and T_{ml} are the right and left motor torques, J_{mr} and J_{ml} are the moment of inertia of right and left motor, J_r and J_l are the moment of inertia of right and left wheel, ω_{mr} and ω_{ml} are the rotational speeds of the right and left motors, γ_r and γ_l are the gear ratios and B_r and B_l are the viscous damping of the right and left wheels.

By combining (4.11) and (4.12) with (4.13) and (4.14), the generated total electromagnetic torque of each electric motor, T_{ml} and T_{mr} , are given in (4.16) and (4.17) [27, 28, 29].

$$T_{mr} = [J_{mr} + \frac{J_r}{\gamma_r^2} + \frac{R_r^2}{2\gamma_r^2} (\frac{M}{2} + \frac{J}{D^2})] \frac{d\omega_{mr}}{dt} + \frac{R_r R_l}{2\gamma_r \gamma_l} (\frac{M}{2} - \frac{J}{D^2}) \frac{d\omega_{ml}}{dt} + \frac{B_r}{\gamma_r^2} \omega_{mr} \quad (4.16)$$

$$T_{ml} = [J_{ml} + \frac{J_l}{\gamma_l^2} + \frac{R_l^2}{2\gamma_l^2} (\frac{M}{2} + \frac{J}{D^2})] \frac{d\omega_{ml}}{dt} + \frac{R_r R_l}{2\gamma_r \gamma_l} (\frac{M}{2} - \frac{J}{D^2}) \frac{d\omega_{mr}}{dt} + \frac{B_l}{\gamma_l^2} \omega_{ml} \quad (4.17)$$

The equations above links torque of the motor with the entire system dynamics parameters with mechanical speed of the motors. This makes a full dynamic expression of the system. It is observed that although the vehicle is differential-drive and the motors are driven independently of each other, the torques given in (4.16) and (4.17) show that the second terms form a coupling between the two motors.

Symmetrical Conditions:

$$R_l = R_r; \quad J_{ml} = J_{mr}; \quad J_l = J_r; \quad \gamma_l = \gamma_r; \quad B_r = B_l \quad (4.18)$$

The system is symmetrical, hence, after applying the symmetrical conditions given above, the self, cross-coupling, and speed coefficients are obtained in (4.19) - (4.23).

$$T_{mr} = A_{self} \frac{d\omega_{mr}}{dt} + A_{cross} \frac{d\omega_{ml}}{dt} + A_{speed} \omega_{mr} \quad (4.19)$$

$$T_{ml} = A_{self} \frac{d\omega_{ml}}{dt} + A_{cross} \frac{d\omega_{mr}}{dt} + A_{speed} \omega_{ml} \quad (4.20)$$

$$A_{self} = [J_{ml} + \frac{J_l}{\gamma_l^2} + \frac{R_l^2}{2\gamma_l^2} (\frac{M}{2} + \frac{J}{D^2})] \quad (4.21)$$

$$A_{cross} = \frac{R_r R_l}{2\gamma_r \gamma_l} (\frac{M}{2} - \frac{J}{D^2}) \quad (4.22)$$

$$A_{speed} = \frac{B_l}{\gamma_l^2} \quad (4.23)$$

4.4 Trajectory Tracking Controller Design

In order to track a trajectory, the system requires information of its present state (x_n, y_n, θ_n) and the next destination state $(x_{n+1}, y_{n+1}, \theta_{n+1})$. This scenario is illustrated in Figure 4-4. It is apparent that orientation at next state, θ_{n+1} , is dependent on current position as given in (4.24).

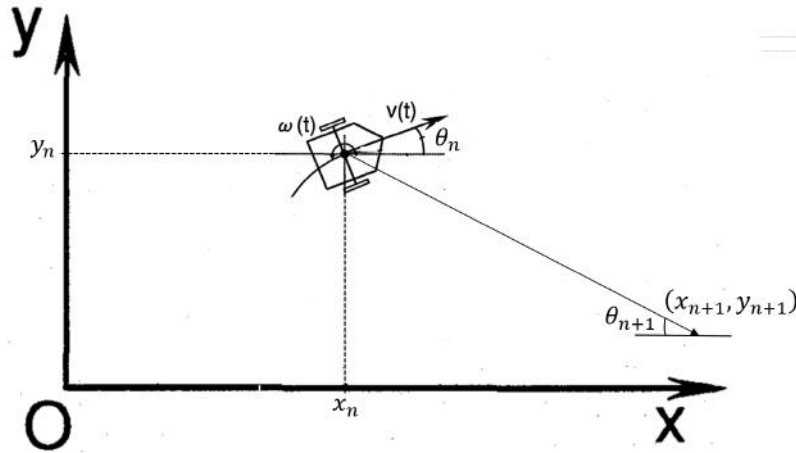


Figure 4-4: Trajectory tracking with destination waypoint

$$\theta_{n+1} = f(x_n, y_n) \quad (4.24)$$

In developing the trajectory tracking algorithm, the distance to the next waypoint and the difference in orientation, as-in a polar coordinate, are pre-processed and continuously fed to individual Proportional-Derivative (PD) controllers. The PD control transfer function, the magnitude of the distance between the two states, and orientation of destination point are given below.

$$TF_{PD} = K_P^T \left(1 + s K_D^T \frac{N}{s + N} \right) \quad (4.25)$$

$$d_n^* = \sqrt{(x_{n+1} - x_n)^2 + (y_{n+1} - y_n)^2} \quad (4.26)$$

$$\theta_{n+1} = \tan^{-1} \frac{y_{n+1} - y_n}{x_{n+1} - x_n} \quad (4.27)$$

where K_P^T and K_D^T are the proportional and differential constants of the PD transfer function, d_n^* is distance to next destination point.

It is expected that the PD controllers will generate speed term corresponding to their respective distance parameter inputs; V^* from linear distance d_n , and ω^* from angular displacement. However, the angular displacements needs more proper adjustments. Two algorithms are detailed below, the first case is used to show the problem while the second case gives a proposed solution. Further details via simulations will be given in section 4.6

Case I:

$$\theta_{dif}^* = \theta_{n+1} - \theta_n \quad \theta_{n+1}, \theta_n \in [-\pi, \pi] \quad (4.28)$$

Case II:

$$\theta_{dif} = \theta_{n+1} - \theta_n \quad \theta_{n+1}, \theta_n \in [0, 2\pi] \quad (4.29)$$

$$\theta_{dif}^* = \begin{cases} \theta_{dif} + (-1)^n 2\pi, & \text{if } |\theta_{dif}| > \pi \\ \theta_{dif}, & \text{otherwise} \end{cases} \quad (4.30)$$

And given that:

$$n = \begin{cases} 1, & \text{if } \theta_{dif} > 0 \\ 2, & \text{if } \theta_{dif} < 0 \end{cases} \quad (4.31)$$

In Case II above, the conditional modulation of θ_{dif}^* removes the problems of sudden large changes in angle signs, maintains vehicle routing through shortest angular rotation, and keeps θ_{dif}^* within $[-\pi, \pi]$ range. These PD controllers then produce the linear and rotational speed references, V^* and ω^* , for the entire vehicle which then is converted to motor speed references, ω_{ml}^* and ω_{mr}^* . This procedure is depicted in Figure 4-5.

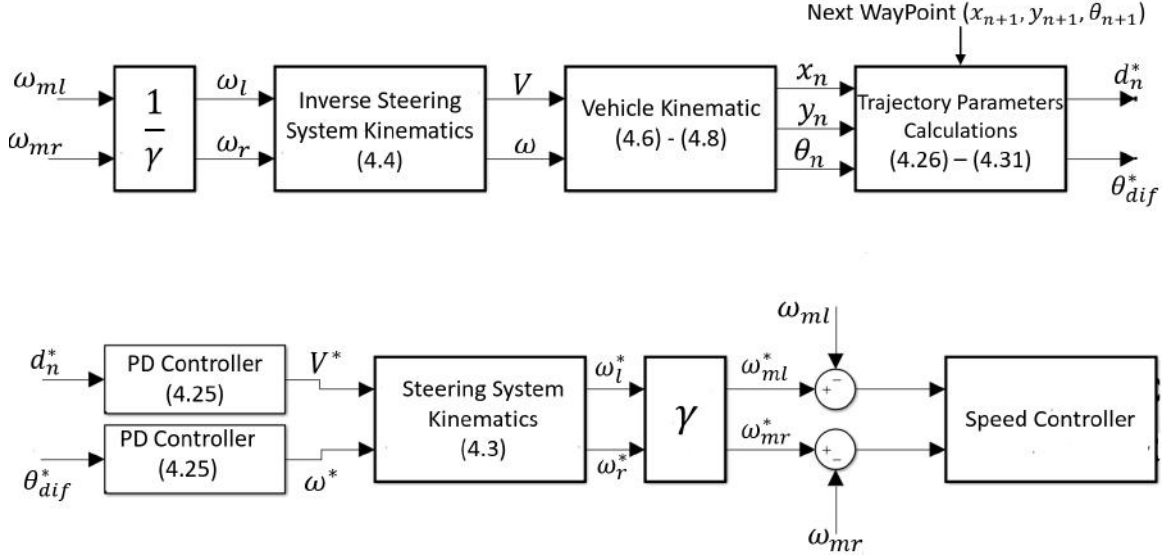


Figure 4-5: Trajectory tracking scheme and procedure

4.5 PMSM Dynamic Modeling and Control

The static models of PMSM are only useful for steady-state analysis, and in order to design controllers and model the effects of transients, the dynamics of the PMSM are required. The dynamics of a PMSM is given in (4.32).

$$\mathbf{v}_{abc} = \mathbf{R}_s * \mathbf{i}_{abc} + \frac{d\boldsymbol{\lambda}_{abc}}{dt} \quad (4.32)$$

$$\boldsymbol{\lambda}_{abc} = \mathbf{L}_s * \mathbf{i}_{abc} + \boldsymbol{\phi}_f \quad (4.33)$$

where \mathbf{v}_{abc} is phase voltage vector at the stator, \mathbf{R}_s is the vector of stator resistance, \mathbf{i}_{abc} is the phase current vector, $\boldsymbol{\lambda}_{abc}$ is the flux linkage at each phase, \mathbf{L}_s is the

vector of phase inductances, and ϕ_f is the flux linkage.

However, as the main function of PMSM control systems in EV applications is instantaneous torque control, the high performance field oriented control (FOC) technique is required. This requires that (4.32)-(4.33) be transformed to the synchronous reference frame in d-q axes. The required Parks transformation matrices and the final PMSM model are given in (4.34) - (4.36). The basic vector control scheme of the PMSM is shown in Figure 4-6. The maximum torque per ampere (MTPA) of surface-mounted PMSM requires that the field producing component of current should be put to zero, $i_d = 0$ [32]. The current and speed controllers designs will be detailed in subsections 4.5.1 and 4.5.2 respectively while that of trajectory controller design is in section 4.4 which is based on the differential drive robot analysis.

$$T(\theta) = \frac{2}{3} \begin{pmatrix} \cos \theta & \cos(\theta - \frac{2\pi}{3}) & \cos(\theta + \frac{2\pi}{3}) \\ -\sin \theta & -\sin(\theta - \frac{2\pi}{3}) & -\sin(\theta + \frac{2\pi}{3}) \\ \frac{1}{2} & \frac{1}{2} & \frac{1}{2} \end{pmatrix} \quad (4.34)$$

$$v_d = R_s * i_d + L_d \frac{di_d}{dt} - \omega_e L_q i_q \quad (4.35)$$

$$v_q = R_s * i_q + L_q \frac{di_q}{dt} + \omega_e L_d i_d + \omega_e \phi_{pm} \quad (4.36)$$

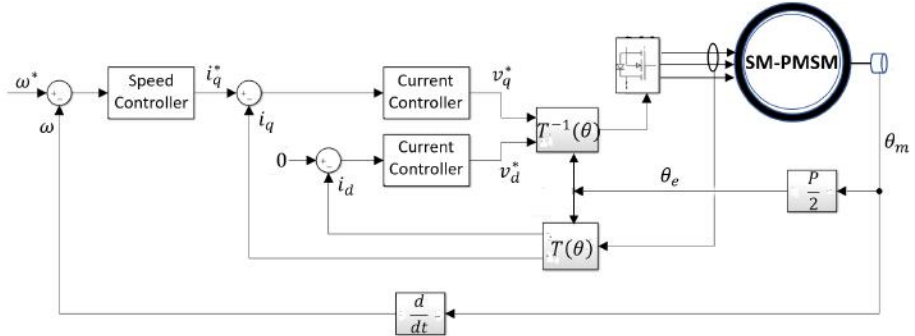


Figure 4-6: Basic vector control scheme of the PMSM

4.5.1 Current Controller Design

The popular Proportional Integral (PI) controller is designed for the current control. The current controller outputs the voltages required to eliminate the current tracking error. However, the coupling terms in (4.35)-(4.36) will affect the voltage outputs of the controllers, hence feedforward decoupling terms are used. The coupling terms are shown in Figure 4-7. This enables the modeling of the stator as mere R-L circuit which simplifies the controller design. Hence, the system and PI controller transfer functions, TF_{elect} and TF_{PI} , are given below.

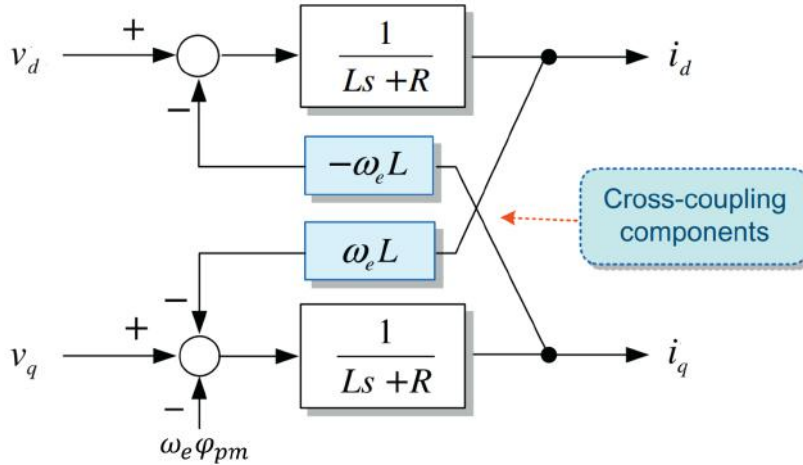


Figure 4-7: PMSM synchronous reference frame model with coupling[32]

$$TF_{elect} = \frac{1}{Ls + R_s} \quad (4.37)$$

$$TF_{PI} = K_P \frac{s + K_I}{s} \quad (4.38)$$

where TF_{elect} is the transfer function of the motor electrical circuit, TF_{PI} is the transfer function of PI controller, K_P and K_I are the proportional and integral constants of the PI controller.

The classical pole-zero cancellation technique used for the control parameters gives values in (4.40). The controller design with the feedforward is shown in Figure 4-8, As shown in Figure 4-8, the voltage outputs are limited by maximum voltage, v_{max}

that the inverter can provide.

$$K_P^i = 2\pi f_c^i L \quad (4.39)$$

$$K_I^i = \frac{R}{L} \quad (4.40)$$

where K_P^i , K_I^i and f_c^i are PI proportional and integral term for the current controller, and the cut-off or bandwidth of the current control loop.

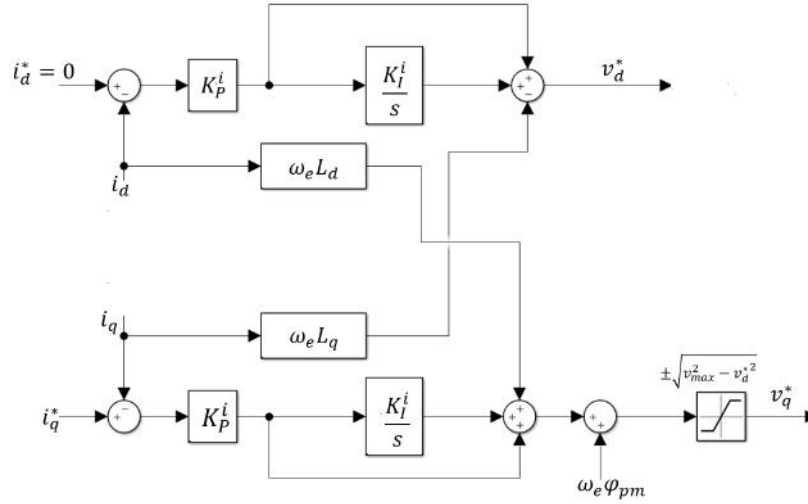


Figure 4-8: Current controller design with feedforward term for decoupling

4.5.2 Speed Controller Design

The speed control loop forms the outer loop in a cascade control system with the current control as the inner loop. The PI control is also used but with a much lesser bandwidth or cut-off frequency. The speed controller requires the dynamics of the vehicle system as seen from the PMSMs, this has been given in (4.19) - (4.20). In order to simplify the controller design, the cross component is neglected in the system transfer function, and used as feedforward. The input to the model is torque while the output is motor speed as given in (4.41). Using the pole-zero cancellation gives PI parameters of (4.42 - 4.43). The speed control design is given in Figure 4-9.

$$TF_{mech} = \frac{1}{A_{self} s + A_{speed}} \quad (4.41)$$

$$K_P^\omega = 2\pi f_c A_{self} \quad (4.42)$$

$$K_I^\omega = \frac{A_{speed}}{A_{self}} \quad (4.43)$$

where K_P^ω , K_I^ω and f_c are PI proportional and integral term for the current controller, and the cut-off or bandwidth of the current control loop.

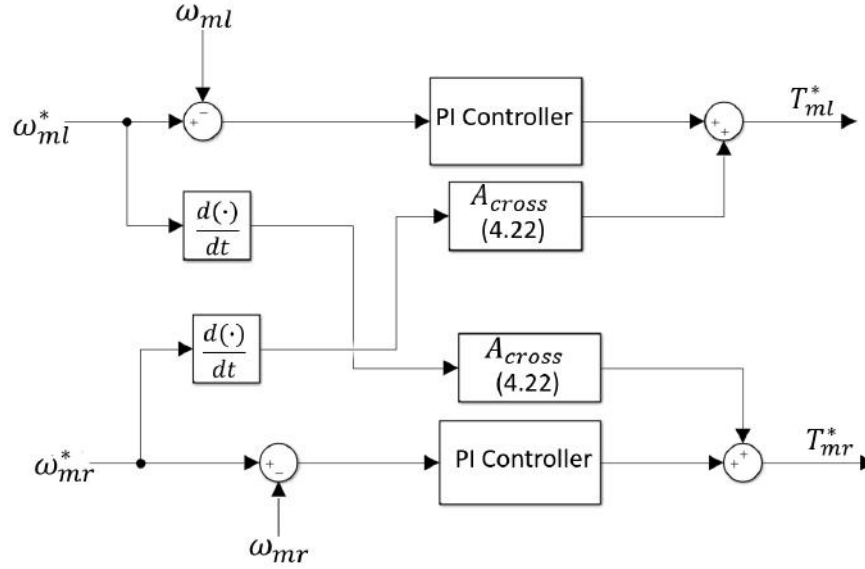


Figure 4-9: Speed controller design with additional feedforward terms

4.6 Path Tracking Simulation Results

Case I and Case II algorithms for trajectory parameter calculations presented in section 4.4 on the trajectory tracking controller design will be put to test herein. Several simulations have been carried-out to determine the performance of the proposed trajectory tracking algorithms and associated design system controllers. First, it is important to showcase the why direct angular differences of Case I do not function properly, thus, motivation for the Case II algorithm. Hence, Figure 4-10 shows the performance of Case I algorithm via the motion behaviour of the vehicle, while Figure 4-11 shows the inherent problem with the angular difference algorithm. All robot visualization graphs are plotted via the MathWorks Robot Simulation Toolbox

v1.0 [33].

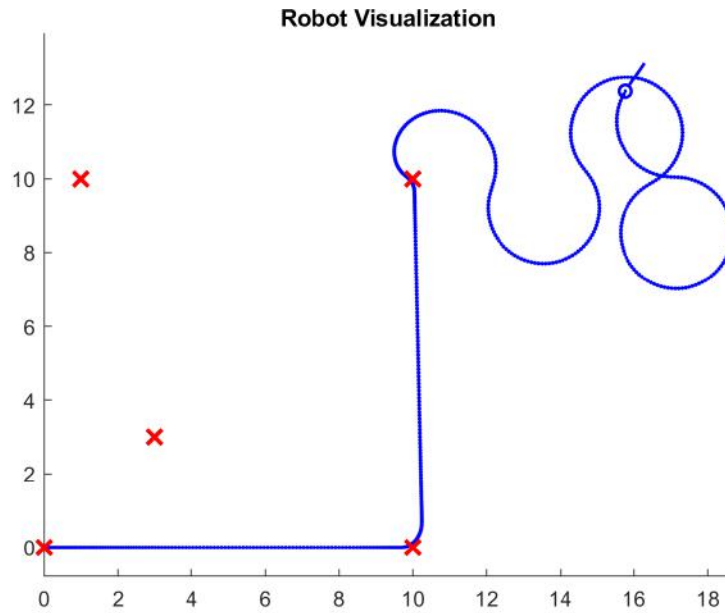


Figure 4-10: Vehicle motion in Case I algorithm

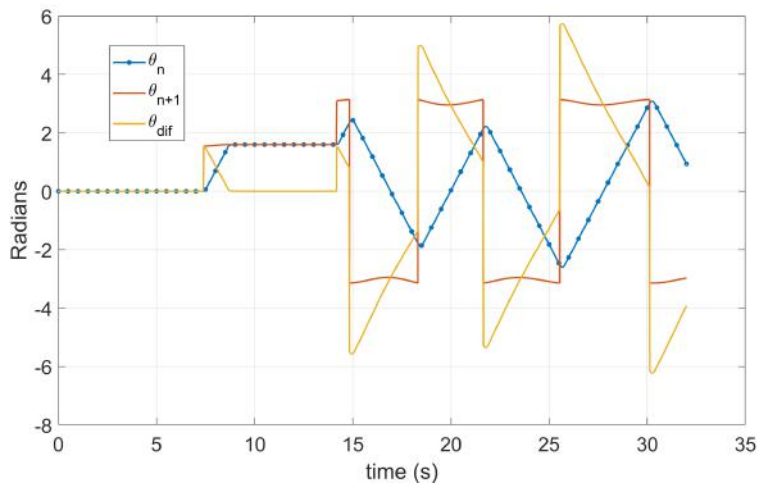


Figure 4-11: Angular difference in motion of Case I algorithm

It can be seen from Figure 4-11 that as soon as the vehicle reaches the 90° angle at about 15 sec, it sees the right angular difference which is approximately $+\pi rad$ s. However, due to inertia, the linear velocity of the vehicle takes the vehicle slightly above the target point, which makes θ_{dif} to switch to approximately $-\pi rad$. This makes the vehicle ω to rotate in the opposite direction, and the cycle repeats again

and again.

The above instability in Case I is solved by algorithm of Case II. The rapid swerve in angular direction of the vehicle is solved by seeking the shortest angle to any target point. This is further aided by the realization that the difference between any two vectors is such that $-\pi \leq \theta_{dif} \leq \pi$, which was maintained by post processing of θ_{dif} based on its initial intrinsic value. Figure 4-12 shows the motion behaviour for Case II while Figure 4-13 gives the angular swerves in this case.

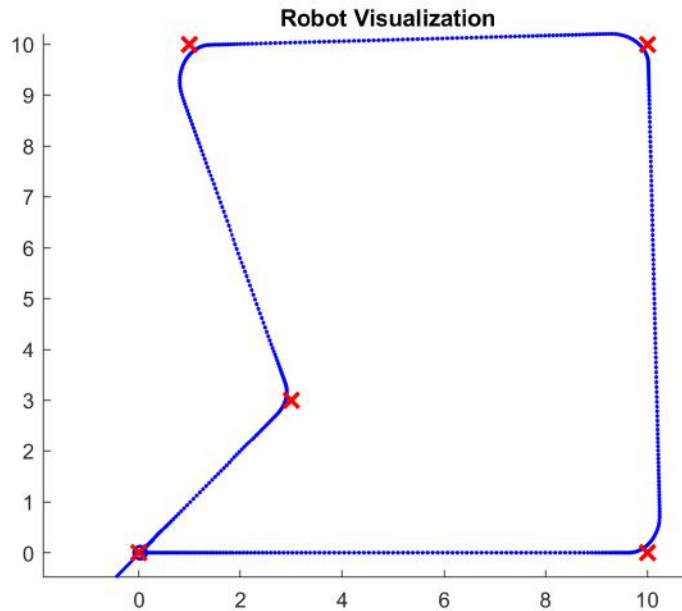


Figure 4-12: Vehicle motion in Case II algorithm

It is in above figures that although θ_n and θ_{n+1} have been given the freedom to vary such that $0 \leq \theta_{dif} \leq 2\pi$, the angular difference has been limited to $-\pi \leq \theta_{dif} \leq \pi$. This is illustrated around $time = 5sec$, Figure 4-13 shows that while $\theta_{n+1} = 2\pi$ and $\theta_n = 0$, $\theta_{dif} = 0$. This removes the incorrect case of making a wrong turn at this point which would have been unnecessary. Hence, the inputs sent into the trajectory tracking controllers, both distance difference (d_n^*) and angular difference (θ_{dif}^*) are graphed in Figure 4-14.

Furthermore, it is worthy of note that the vehicle receives data for the next destination point, (x_{n+1}, y_{n+1}) , in the waypoint only when it gets very close to its present destination, (x_n, y_n) . hence, it is apparent that there will be sharp bursts of velocity

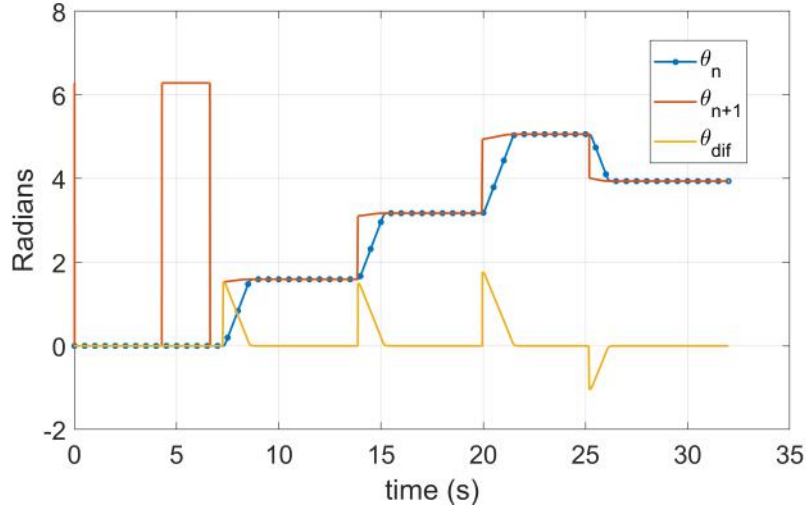


Figure 4-13: Angular difference in motion of Case II algorithm

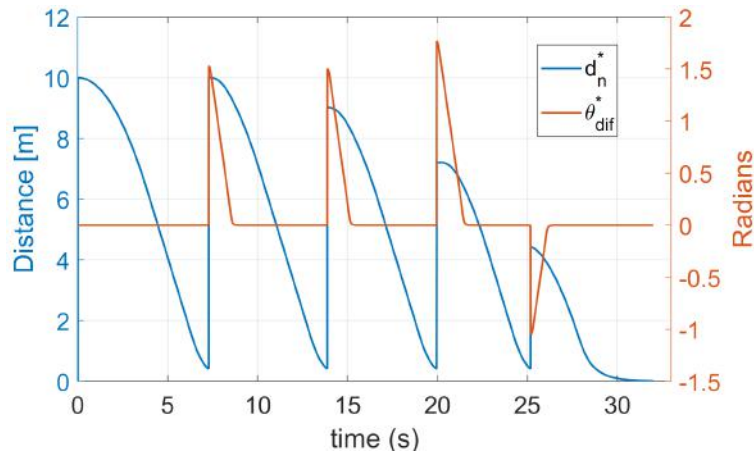


Figure 4-14: Error inputs into trajectory tracking controllers

changes of the vehicle, V and ω , at the point of next destination view (NDV). The velocities of the vehicle are given in Figure 4-15. Efforts are also made to limit these velocities in order to account for the physical limits in the speeds of the receiving end PMSM motors.

It can be viewed in Figure 4-15 the rate of decrease in linear velocity or linear deceleration is faster than that of linear acceleration while angular acceleration and angular deceleration are made to be even faster, this is made to allow faster turning and bending of the vehicle at corner points. This also enable better position control and straight line alignment. These linear and angular accelerations of the vehicle in

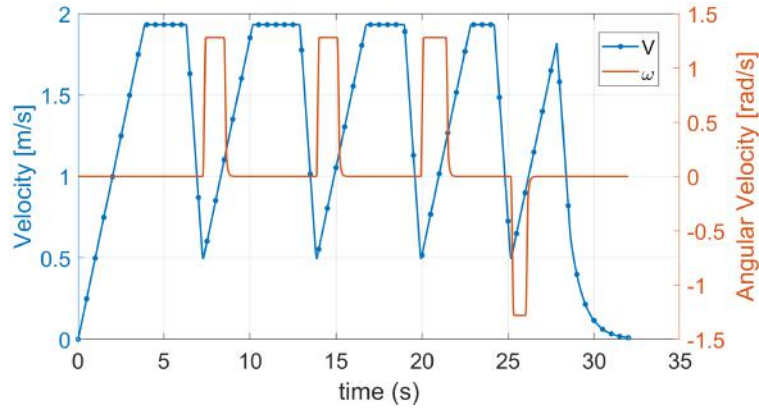


Figure 4-15: Linear and angular velocities of vehicle

this time frame are shown in Figure 4-16.

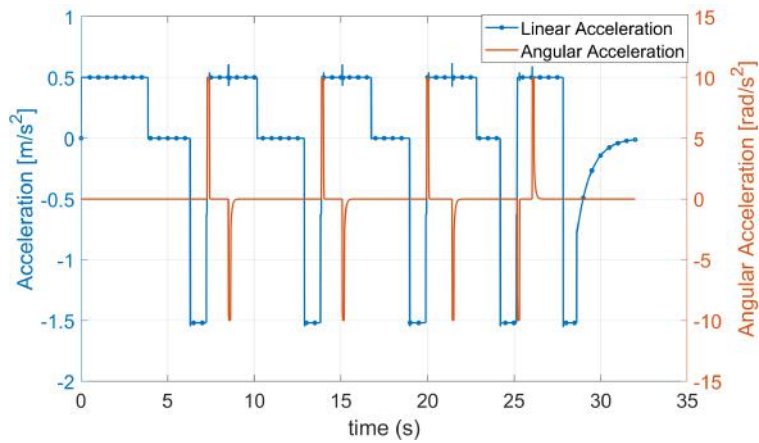


Figure 4-16: Linear and angular acceleration of vehicle

The jerking of the vehicle which is a derivative of its acceleration is also presented in Figure 4-17. This is necessary mostly for vibration analysis and comfortability, but in case of this unmanned vehicle, it will be about the amount of torque required in bolts, nuts and screws in order to reduce maintenance cost and increase overall system reliability.

The vehicle linear and angular velocities are further converted to the PMSM motors' speeds via the kinematic models. The simulation does not place any direct simulation limits discontinuities on the motor speeds. The speed of each PMSM is given in Figure 4-18. More so, the global position of the vehicle as it moves in its path is also given in Figure 4-19.

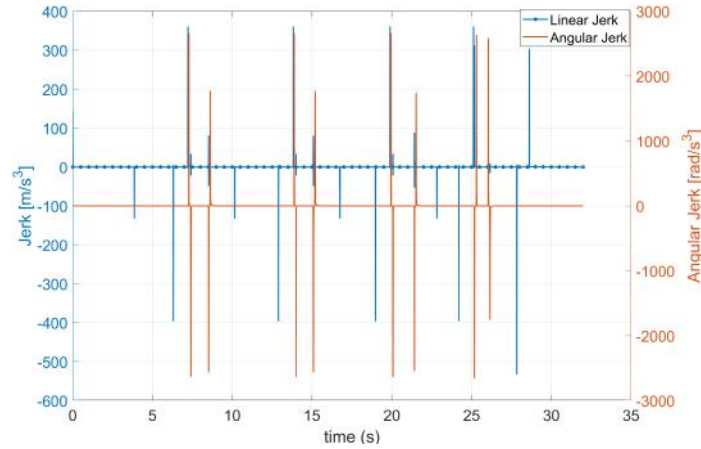


Figure 4-17: Linear and angular jerk of vehicle

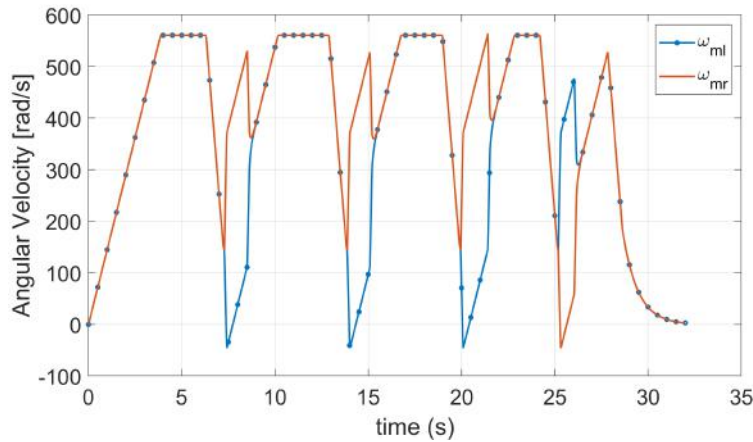


Figure 4-18: Speed of PMSM motors of vehicle

It is seen that there are some points high speed changes in the speed of the electric motors, although not physical possible, this high rises and drops will require huge torques from each electric motor and hence currents. Although they are for very short periods, the torques for both right and left motors are shown in Figure 4-20

In the torque figure, the sharp turnings require more than the rated torque of the PMSM but far less than the overload torque. This will lead to huge current demands from each motors at different turns. The current demand profiles for the left and right electric motors are shown in Figures 4-21 and 4-22 respectively. The output of the current control loop will require voltage response to eliminate the current loop errors. This voltage commands given to inverters are therefore given in Figures 4-23 - 4-24.

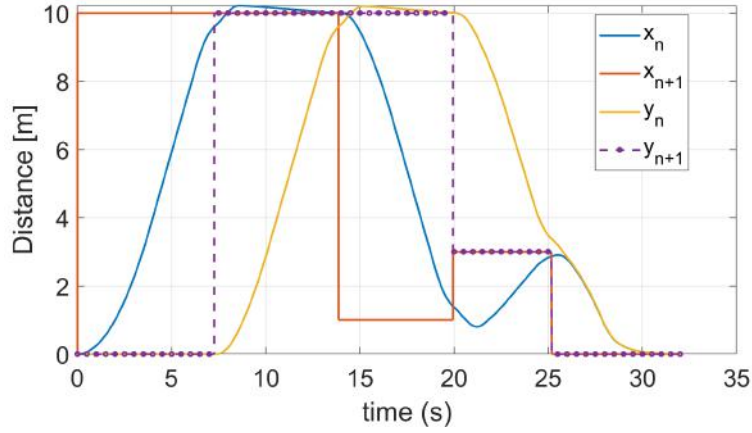


Figure 4-19: Vehicle position in global coordinates with next-point commands

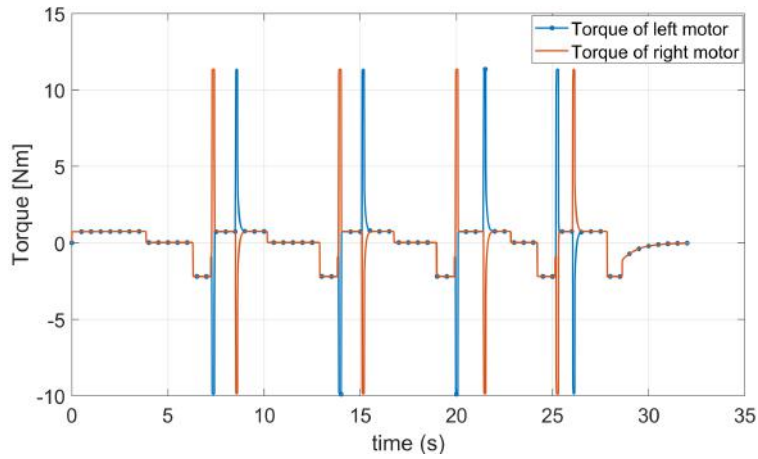


Figure 4-20: Torque of right and left electric motors of vehicle

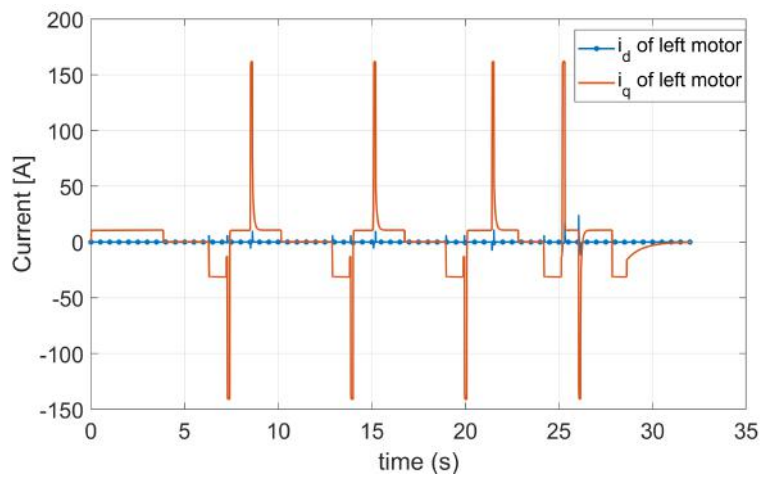


Figure 4-21: Current of left motor of vehicle

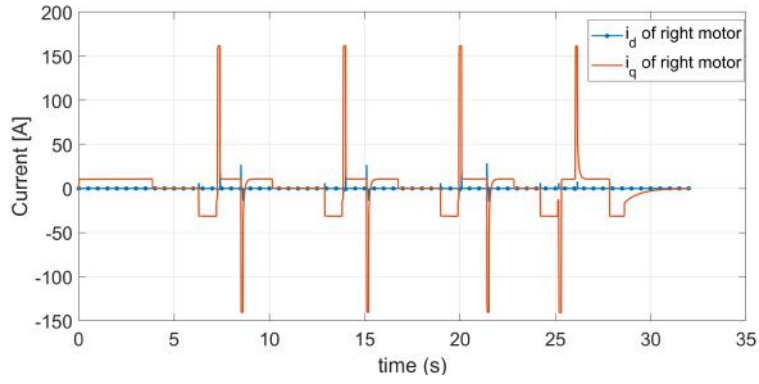


Figure 4-22: Current of right motor of vehicle

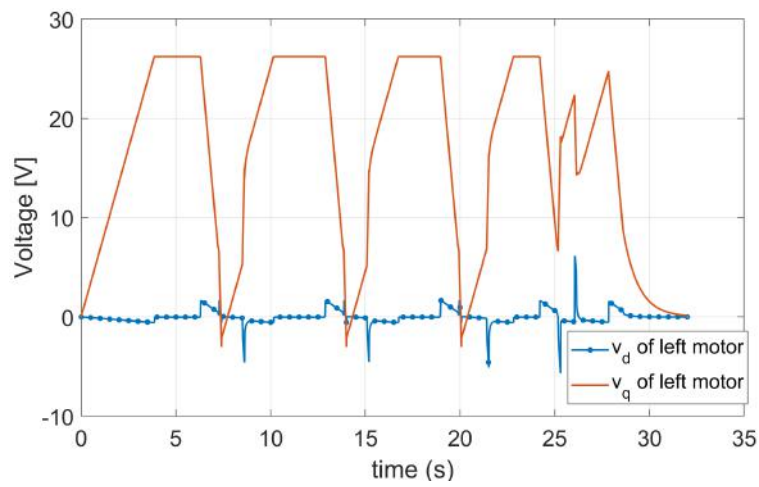


Figure 4-23: Voltage of left motor of vehicle

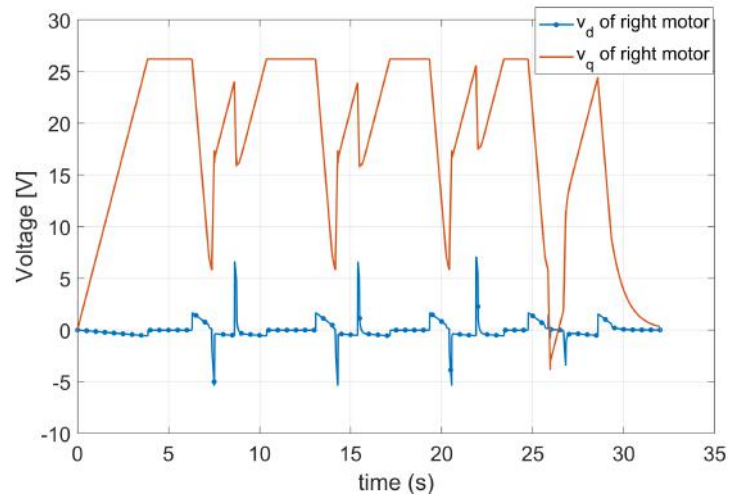


Figure 4-24: Voltage of right motor of vehicle

4.7 Conclusion

This chapter has shown that with the simple proportional-derivative controller and intelligent measure of angular difference, as-in a polar coordinate styled control scheme, it is possible to design an efficient trajectory tracking autonomous vehicle. The trajectory tracking algorithm is successfully integrated with the speed and control controls of the proposed dual-motor series hybrid electric vehicle. However, it is worthy of note that only flat surfaces have been considered so far in the simulations. More so, a typical map-out of a farmland will be larger and more complicated than shown in Figures 4-12 and 4-10

The proposed trajectory is tried on the given real-farm layout (figure withheld for propriety issues) and it shows some level of success with some imperfections. The path followed by the vehicle is shown in Figure 4-25 while the angular difference is shown in Figure 4-26 It is seen that at about 87 sec, there is a problem with sharp angular instability, this is caused by the high speed of the right wheel motor which was gained to turn the machine in the right direction and maintained by inertia which drags the machine. However, the vehicle recovers in a second attempt. The speed of the motors are given in Figure 4-27 and it can be seen that right motors exceed the motor speed limits at about the same time of 87 sec. Without doubt, the scheme as potentials which can be improved to work perfectly in farms.

**THIS PAGE IS INTENTIONALLY LEFT BLANK FOR PROPRIETY
CLAIMS OF SVMAC INGENIERIA SISTEMAS Y VEHICULOS**

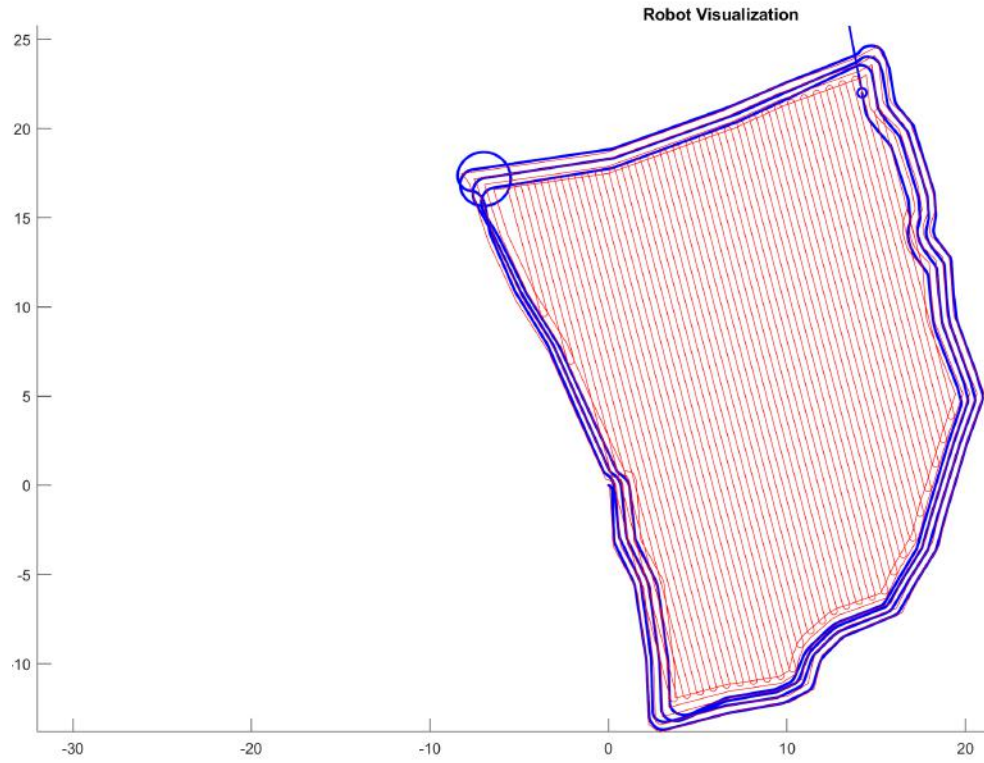


Figure 4-25: Vehicle motion in case of real farmland trajectory

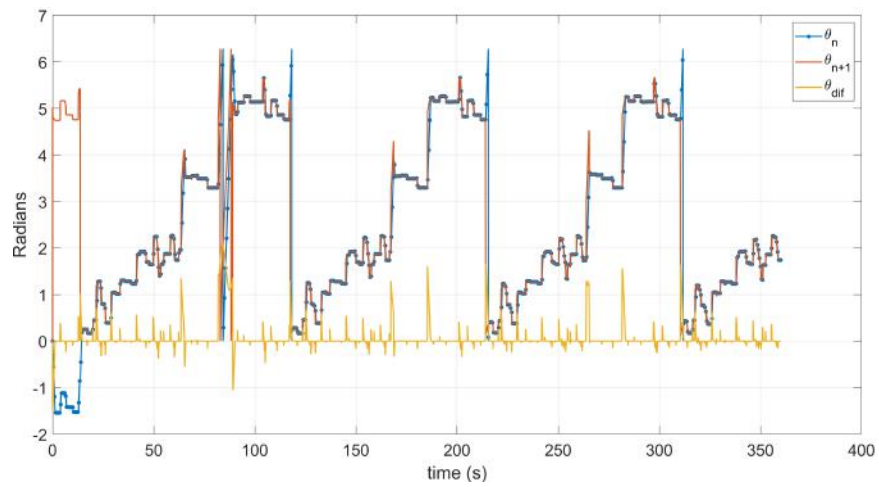


Figure 4-26: Angular difference in case of real farmland trajectory

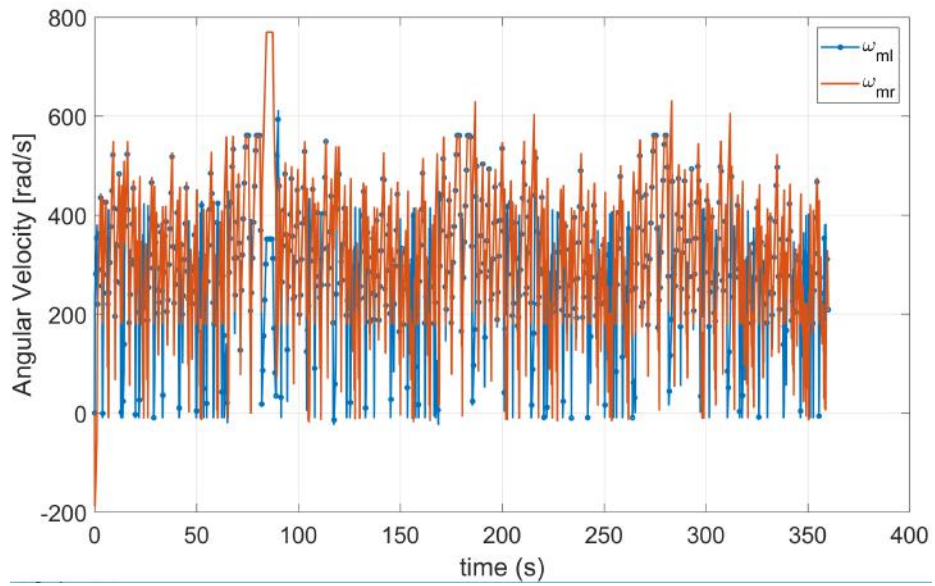


Figure 4-27: Speed of PMSM motors of vehicle in case of real farmland trajectory

Chapter 5

Experimental Set-Up

The laboratory experimental setup of the proposed series hybrid electric vehicle is explored in this chapter as laid out in section 3.2 of Chapter 3. Furthermore, the results from the practical implementation of the system are given in this chapter.

5.1 Platform Assembly

It is worthy of mention that this platform assembly was entirely started by me, with my adviser's guidelines and manufacturer's manuals, from hacking how to interact with the first inverter, cabling its special terminals, connecting with motors, and so on. However, as the project was massive and required more hands, two PhD students were assigned to assist in the final stages of the microcontroller programming corrections, bottlenecks and sensor calibrations.

In order to assemble the platform for a laboratory environment few improvisations expedient for the course are necessary. The entire platform with all accessories to operate is shown in Figure 5-1. In this figure, the entire platform is divided into three sections based on the components; Engine, Generator and Motor bench, DC/AC Inverter, Master and Remote Controller bench and DC/DC Converter and Battery bench. Furthermore, it is worthy of note that some compromise have been made regarding the components, this and each bench will be exploited in details below.

- The Internal combustion engine has been replaced by an AC induction motor

for laboratory purpose as the main prime mover. Also, it does not have any mechanical load, hence, it drives only a generator which provides electrical power for the inverter and DC/DC converter. This AC motor is controlled by a commercial drive shown in Figure 5-5.

- The laboratory platform lacks access to load parameters, such as mass of vehicle, moment of inertia, and ground resistance, necessary to create load torque for the PMSM motors. Hence, motors are connected to the driving PMSM motors to provide load torque.
- Rather than using individual DC/AC inverter for each PMSM, a dual three-Phase commercial inverter containing six half-bridges is employed to use 3 legs for each PMSM. The inverter has internal TI TMS320F28335 Microcontroller, current, voltage and temperature sensors, and 43.2mF dc-link capacitor.
- Similar to the inverter, the DC/DC converter is a commercial product with TI TMS320F28335 Microcontrollers, current, voltage and temperature sensors, and a dc-link capacitor. However, it is a single three phase inverter which is used as dc/dc converter for each batteries as shown in Figure 5-4. To do this, each leg of the inverter is used as low voltage input where an inductor and battery are connected, while the dc-link acts as the high-voltage terminal where the generator is connected. Just two of the three legs of the inverter are used.
- The remote controller, receiver and transmitter, are commercial products. The receiver physically communicates via CAN with the master controller.
- The Master controller is composed of a Raspberry Pi module and a Texas Instrument TMS320F28335 Microcontroller. The Raspberry PI is used for data-acquisition and processing , such as from the remote and trajectory path planner, while the TMS320F28335 Microcontroller does all the real-time control and supervision of entire platform.
- All the control systems designed in the thesis are implemented in C in the TMS320F28335 Microcontrollers; the trajectory path tracking control design

is implemented in the master control which then sends speed commands to inverter. The inverter and the DC/DC converter house their respective control designs.

The graphical details of each bench are given to clearer glare in Figures 5-2 - 5-4.

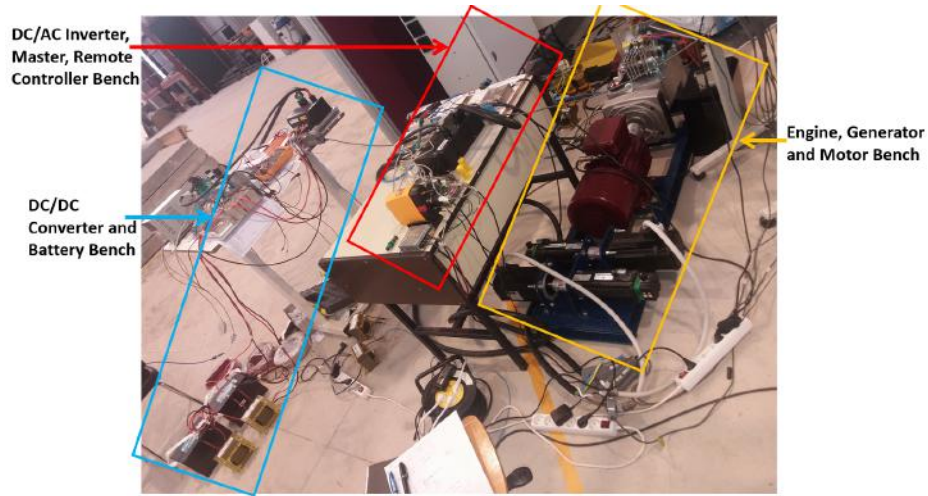


Figure 5-1: Entire platform with all accessories

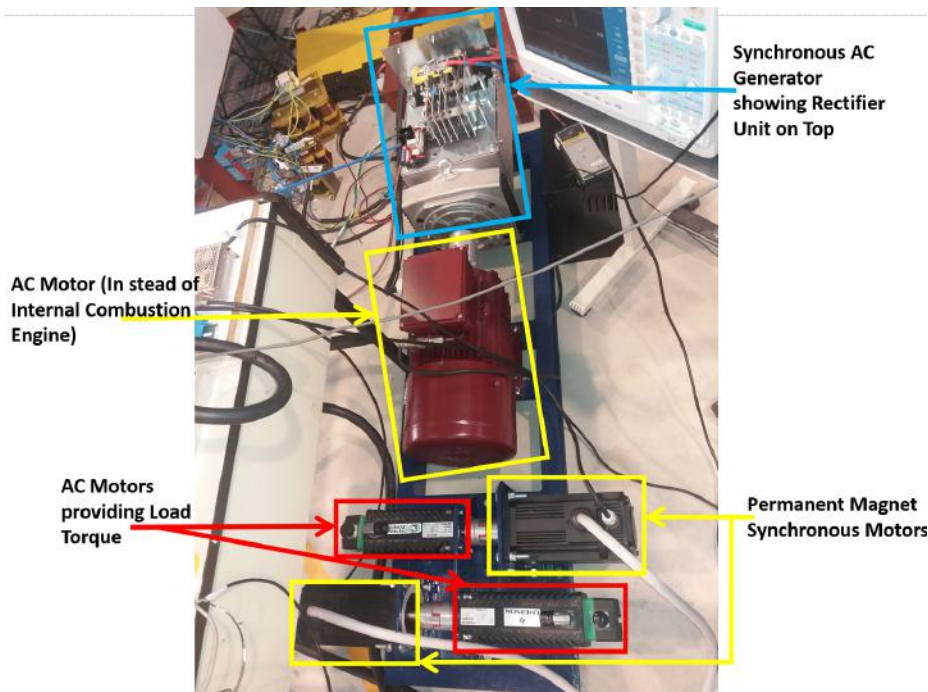


Figure 5-2: Engine, generator and motor bench

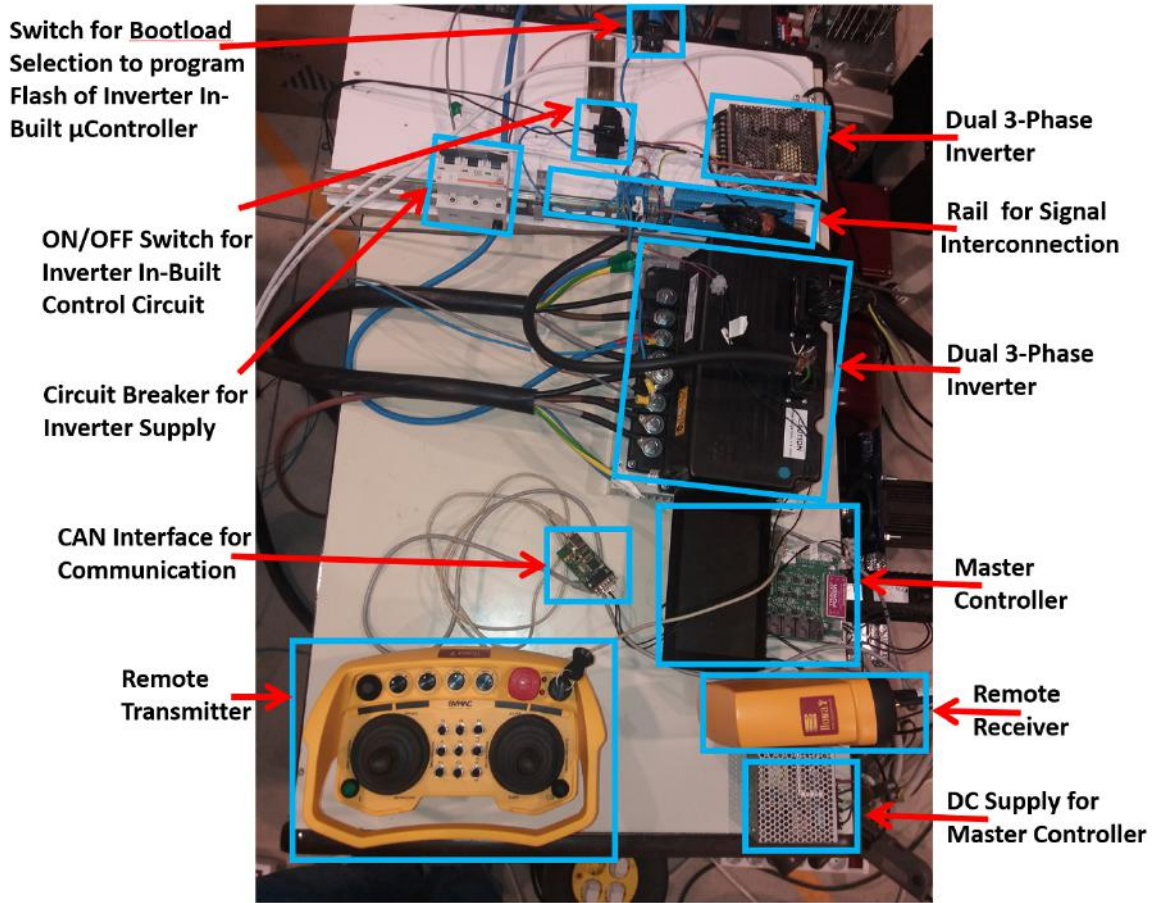


Figure 5-3: DC/AC inverter, master controller and remote controller bench

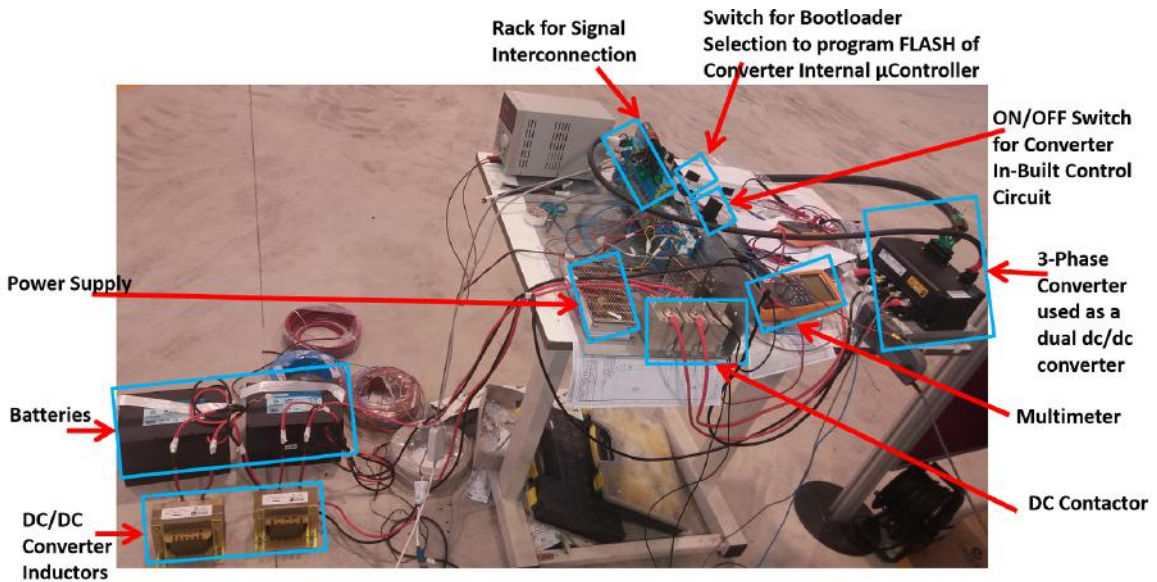


Figure 5-4: DC/DC converter and battery bench



Figure 5-5: Commercial electric drive for prime mover

5.2 Experimental Results

After coupling the entire system, the mechanism of operation of the system is explored. The motors are controlled to move at speeds of 150rad/s for PMSM-2 and 75rad/s for PMSM-1 and observed. The ac currents at the input phases of the two motors and the dc-link voltage are measured and displayed via oscilloscope. The current control system of the battery was also tested and response of the batteries as a unit is also captured. This plot is shown in Figure 5-6. In the figure, the effect of high frequency switching at 10kHz can be seen on the currents' waveform.

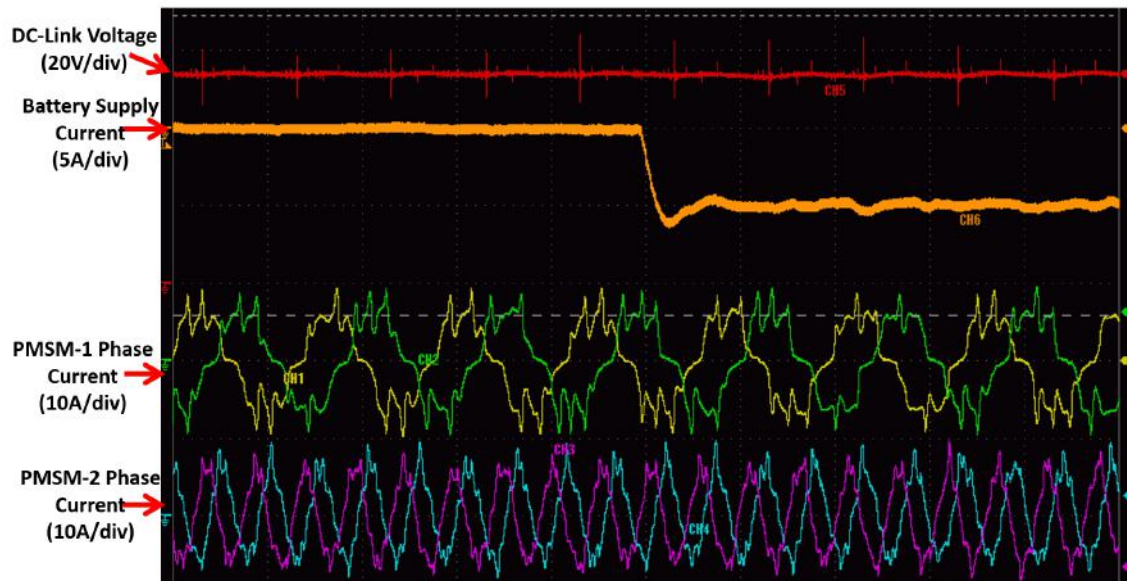


Figure 5-6: Experimental results

Chapter 6

Conclusions and Future Works

It is highly popular that electricity is the new fuel for vehicles leading to the massive attention received by electric vehicular transportation especially the train system and personal car system. These thesis has joined the charade of expanding the electric take-over revolution towards new applications, agricultural application in this case. However, several issues, challenges and milestones still need to be reached in this revolution. This chapter gives details of points reached in this thesis and possible future horizons.

6.1 Conclusions

For the most part, this thesis has been largely based on the design of several controllers, and integration of several technologies to successfully build a hybrid electric vehicle with autonomous capability and ability to be remotely controlled. Herein, the conclusive points are itemized and presented.

- A favourable series hybrid electric vehicle topology suitable in precision agricultural farming has been proposed and analyzed. The system is successfully simulated and performance is checked. The topology had passed through first-stage implementation in the laboratory and is shown that all components are successfully coupled.

- An efficient energy management system has been designed to cater for balance of prioritized operations. It is shown that the EMS recognizes the time and needs of the mechanical pump which is prioritized power demand.
- A successful trajectory tracking planning scheme has been designed. The trajectory parameters calculation and PD controllers have been successful tuned for favourable response. The trajectory tracking control system has been successfully integrated with the control systems of the motors.
- The entire vehicle system dynamics and kinematics, and steering system kinematics have been detailed and served as an interconnection between the trajectory planning and control system of the vehicle with the combined dynamics of the wheel and electric motors.
- The low bandwidth speed control loop system and high bandwidth current loop control system has been designed for each electric motor taking into consideration the entire vehicle mass, moment of inertia, those of the wheels, and forces required to move the vehicle.
- The autonomous function of the proposed vehicle is shown to be achievable via integration of geolocation mapping of farms via RTK GPS systems and the proposed trajectory tracking controller system designed in this thesis.

6.2 Future Works

Although, the proposed series HEV has been largely successful in simulation and laboratory environment, there are several points of improvements that can be implemented. A list of possible future development dimensions are given, however, it is to be noted that this list is not exhaustive.

- The electric vehicle platform can be developed into a ready-to-farm hybrid electric vehicle with all the proposed features.

- In this thesis, only the two-dimensional flat-surface simulations have been made. This can be expanded to three-dimensional hilly-surface simulations to show case the real cases of vast landscapes of different farms. Hence, making the vehicle more universal in application.
- Although, the designed platform has autonomous capabilities, it cannot by itself observe advanced functions such as object avoidance, potholes maneuver, and resisting to cut trees or animals. Hence, artificial intelligence capabilities can be integrated into the system.
- For more flexibility the vehicle can be upgraded to plug-in such as the battery can be given some head. More so, the vehicle can be made more sustainable by eliminating the internal combustion by converting from hybrid series to full electric vehicle or fuel cell electric vehicle.

Appendix A

Tables

Table A.1: Bi-directional DC/DC Converter Parameters

Parameter	Value
V_{Batt}	24V
R_L	0.06 Ω
L	12vmH
R_{T1}	1.6 m Ω
V_{T1}	1V
V_D	1.2 V

Table A.2: Permanent Magnet Synchronous Motor Data

Parameter	Value
R_s	0.007469 Ω
L_d	0.0002679 H
L_q	0.0003203 H
K_t	0.07012 Nm/A
Poles	6
$J_{ml=J_{rl}}$	0.00076359 Kgm ²
ϕ_{PM}	0.15608 Vs

Table A.3: Vehicle and Dynamics Data Used in Simulation

Parameter	Value
$R_l = R_r$	0.1723m
M	700kg
D	1.125m
γ	50
J	602 Kgm^2
$J_l = J_r$	0.2342 Kgm^2
$B_l = B_r$	0.1 Nms
A_{self}	0.0058 Nms^2
A_{speed}	0.00004 Nms^2
A_{cross}	-00074607 Nms

Table A.4: Controller Design Parameters

Parameter	Value
$f_{c,Batt}^i$	500 Hz
$K_{P,Batt}^i$	37.6991
$K_{I,Batt}^i$	5
f_c^i	310 Hz
K_P^i	0.048
K_I^i	302.6178
f_c^ω	50 Hz
K_P^ω	1.8094
K_I^ω	0.0069
$K_P^T(\text{linearspeed})$	3.3472
$K_D^T(\text{linearspeed})$	0.2477
$K_P^T(\text{Angularspeed})$	12.8556
$K_D^T(\text{Angularspeed})$	0.000164

Appendix B

Figures

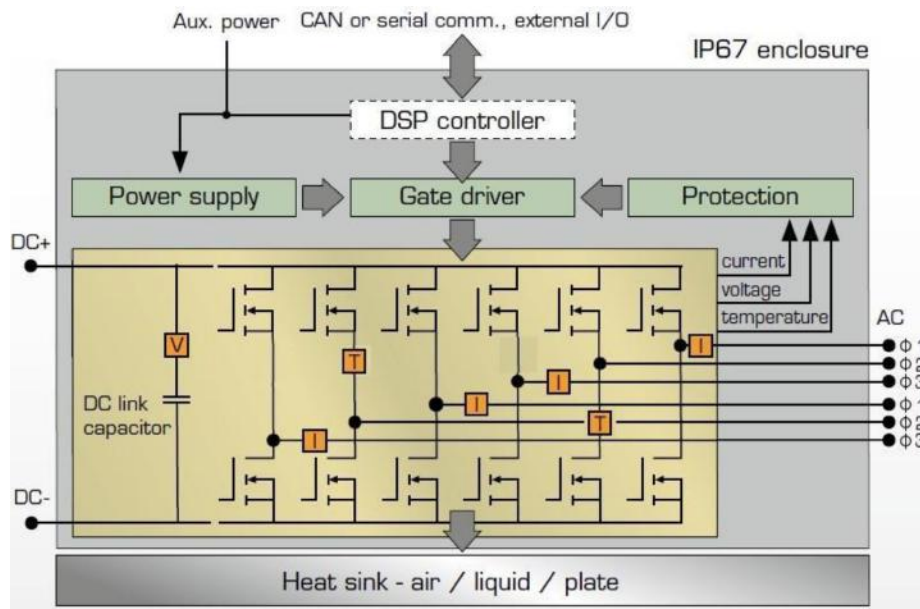


Figure B-1: Internal features of SKAI2 LV A2 MM10-L MOSFET inverter [34]



Figure B-2: Package outlook of SKAI2 LV A2 MM10-L MOSFET inverter [34]

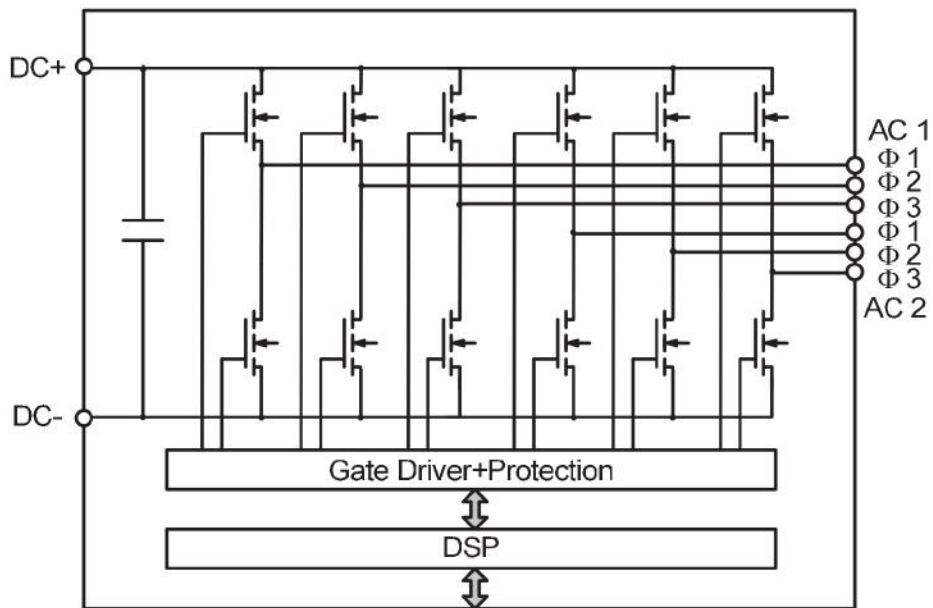


Figure B-3: Dual three-phase MOSFET inverter as connection point for the PMSMs [35]



Figure B-4: ACM BRL110-3D 6 Poles Permanent Magnet Synchronous Electric Motor



Figure B-5: Sincro FB 4-48/150 Brushless Synchronous Generator with DC output

Bibliography

- [1] Friederike Wagner, Sjoerd J. P. Bohncke, David L. Dilcher, Wolfram M. Kürschner, Bas van Geel, and Henk Visscher. Century-scale shifts in early holocene atmospheric co2 concentration. *Science*, 284(5422):1971–1973, 1999.
- [2] Joshua P. Howe. This is nature; this is un-nature: Reading the keeling curve. *Environmental History*, 20(2):286–293, 2015.
- [3] J.P. Rodrigue, C. Comtois, and B. Slack. *The Geography of Transport Systems*. Taylor & Francis, 2016.
- [4] U.S. Energy Information Administration. Energy use for transportation. https://www.eia.gov/energyexplained/index.php?page=us.energy_transportation, May 2018.
- [5] European Environment Agency. Final energy consumption by sector and fuel. <https://www.eea.europa.eu/data-and-maps/indicators/final-energy-consumption-by-sector-9/assessment-1>, January 2017.
- [6] Shumei Cui, Shouliang Han, and C. C. Chan. Overview of multi-machine drive systems for electric and hybrid electric vehicles. In *2014 IEEE Conference and Expo Transportation Electrification Asia-Pacific (ITEC Asia-Pacific)*, pages 1–6, Aug 2014.
- [7] A. Emadi, K. Rajashekara, S. S. Williamson, and S. M. Lukic. Topological overview of hybrid electric and fuel cell vehicular power system architectures and configurations. *IEEE Transactions on Vehicular Technology*, 54(3):763–770, May 2005.
- [8] X. Zhang and C. Mi. *Vehicle Power Management: Modeling, Control and Optimization*. Power Systems. Springer London, 2011.
- [9] J. Cao and A. Emadi. A new battery/ultracapacitor hybrid energy storage system for electric, hybrid, and plug-in hybrid electric vehicles. *IEEE Transactions on Power Electronics*, 27(1):122–132, Jan 2012.
- [10] Sang-Hoon Kim. Chapter 4 - modeling of alternating current motors and reference frame theory. In Sang-Hoon Kim, editor, *Electric Motor Control*, pages 153 – 202. Elsevier, 2017.

- [11] Dura Magnetics Inc. Alnico magnets for high heat applications. Available online at <https://www.duramag.com/techtalk/alnico-magnets/alnico-magnets-for-high-heat-applications>, December 2014.
- [12] M. Zeraouia, M. E. H. Benbouzid, and D. Diallo. Electric motor drive selection issues for hev propulsion systems: A comparative study. *IEEE Transactions on Vehicular Technology*, 55(6):1756–1764, Nov 2006.
- [13] G. Pellegrino, A. Vagati, B. Boazzo, and P. Guglielmi. Comparison of induction and pm synchronous motor drives for ev application including design examples. *IEEE Transactions on Industry Applications*, 48(6):2322–2332, Nov 2012.
- [14] Z. Yang, F. Shang, I. P. Brown, and M. Krishnamurthy. Comparative study of interior permanent magnet, induction, and switched reluctance motor drives for ev and hev applications. *IEEE Transactions on Transportation Electrification*, 1(3):245–254, Oct 2015.
- [15] X. Liu, H. Chen, J. Zhao, and A. Belahcen. Research on the performances and parameters of interior pmsm used for electric vehicles. *IEEE Transactions on Industrial Electronics*, 63(6):3533–3545, June 2016.
- [16] Dura Magnetics Inc. Magnets in the news: Recent developments in rare earth element supply. Available online at <https://www.duramag.com/techtalk/magnet-news/magnets-in-the-news-recent-developments-in-rare-earth-element-supply>, May 2018.
- [17] A. Yamada and I. Miki. New permanent magnet synchronous motor with reduced rare earth magnets. In *2014 17th International Conference on Electrical Machines and Systems (ICEMS)*, pages 391–396, Oct 2014.
- [18] P. Sekerak, V. Hrabovcova, J. Pyrhonen, L. Kalamen, P. Rafajdus, and M. Onufer. Comparison of synchronous motors with different permanent magnet and winding types. *IEEE Transactions on Magnetics*, 49(3):1256–1263, March 2013.
- [19] W. Zhao, T. A. Lipo, and B. Kwon. Comparative study on novel dual stator radial flux and axial flux permanent magnet motors with ferrite magnets for traction application. *IEEE Transactions on Magnetics*, 50(11):1–4, Nov 2014.
- [20] Armeva european project. Available online at <http://www.armeva-project.eu/>, May 2018.
- [21] T. Finken, M. Hombitzer, and K. Hameyer. Study and comparison of several permanent-magnet excited rotor types regarding their applicability in electric vehicles. In *2010 Emobility - Electrical Power Train*, pages 1–7, Nov 2010.
- [22] D. Trajkovski and G. Cvetkovski. Performance analysis of different rotor topologies in permanent magnet motor. In *IEEE EUROCON 2017 -17th International Conference on Smart Technologies*, pages 411–416, July 2017.

- [23] G. I. Vakil and K. R. Rajagopal. Performance comparison of sinusoidally-fed pm bldc motors having different rotor topologies. In *2010 Joint International Conference on Power Electronics, Drives and Energy Systems 2010 Power India*, pages 1–5, Dec 2010.
- [24] Y. Liu, D. Cheng, J. Bai, C. Tong, Z. Song, and W. Tong. Topology comparison of compound-structure permanent-magnet synchronous machines. *IEEE Transactions on Industry Applications*, 48(6):2217–2222, Nov 2012.
- [25] Z. Xuhui, X. Wen, Z. Feng, and G. Xinhua. A new control strategy for bi-directional dc-dc converter in electric vehicle. In *2011 International Conference on Electrical Machines and Systems*, pages 1–4, Aug 2011.
- [26] R.W. Erickson and D. Maksimovic. *Fundamentals of Power Electronics*. Power electronics. Springer US, 2001.
- [27] S. Iida and S. Yuta. Control of a vehicle subsystem for an autonomous mobile robot with power wheeled steerings. In *Proceedings of the IEEE International Workshop on Intelligent Motion Control*, volume 2, pages 859–866, Aug 1990.
- [28] P. García, J. A. Cancelas, and V. M. González. Collaborative subjects for embedded systems learning in the ehea frame: A practical approach. In *IEEE EDUCON 2010 Conference*, pages 1255–1264, April 2010.
- [29] S. Iida and S. Yuta. Control of vehicle with power wheeled steering using feed-forward dynamics compensation. In *Proceedings IECON '91: 1991 International Conference on Industrial Electronics, Control and Instrumentation*, pages 2264–2269 vol.3, Oct 1991.
- [30] S. Iida and S. Yuta. Vehicle command system and trajectory control for autonomous mobile robots. In *Proceedings IROS '91:IEEE/RSJ International Workshop on Intelligent Robots and Systems '91*, pages 212–217 vol.1, Nov 1991.
- [31] C. B. Low. A trajectory tracking control scheme design for nonholonomic wheeled mobile robots with low-level control systems. In *2012 IEEE 51st IEEE Conference on Decision and Control (CDC)*, pages 536–543, Dec 2012.
- [32] Sang-Hoon Kim. Chapter 6 - current regulators of alternating current motors. In Sang-Hoon Kim, editor, *Electric Motor Control*, pages 247 – 264. Elsevier, 2017.
- [33] MathWorks Student Competitions Team. Mobile robotics simulation toolbox v1.0.0.0. <https://uk.mathworks.com/matlabcentral/fileexchange/66586-mobile-robotics-simulation-toolbox>, March 2018.
- [34] Lutz Görgens and Alexander Fries. *SKAI2 LV Dual 3-Phase Inverter Technical Explanation Manual*. SemiKron, December 2016.
- [35] SemiKron. *SKAI2 60 A2 MM10-L Datasheet*, November 2017.